

1-1-2014

Segregation of Particles of Variable Size and Density in Falling Suspension Droplets

Melissa Kathleen Faletra
University of Vermont, mkfaletr@gmail.com

Follow this and additional works at: <http://scholarworks.uvm.edu/graddis>

 Part of the [Mechanical Engineering Commons](#), and the [Physics Commons](#)

Recommended Citation

Faletra, Melissa Kathleen, "Segregation of Particles of Variable Size and Density in Falling Suspension Droplets" (2014). *Graduate College Dissertations and Theses*. Paper 265.

This Thesis is brought to you for free and open access by the Dissertations and Theses at ScholarWorks @ UVM. It has been accepted for inclusion in Graduate College Dissertations and Theses by an authorized administrator of ScholarWorks @ UVM. For more information, please contact donna.omalley@uvm.edu.

SEGREGATION OF PARTICLES OF VARIABLE SIZE AND DENSITY IN
FALLING SUSPENSION DROPLETS

A Thesis Presented

by

Melissa Faletra

to

The Faculty of the Graduate College

of

The University of Vermont

In Partial Fulfillment of the Requirements
for the Degree of Master of Science
Specializing in Mechanical Engineering

October, 2014

Accepted by the Faculty of the Graduate College, The University of Vermont, in partial fulfillment of the requirements for the degree of Master of Science, specializing in Mechanical Engineering.

Thesis Examination Committee:

Jeffrey Marshall, Ph.D. Advisor

Yves Dubief, Ph.D.

Christopher Danforth, Ph. D. Chairperson

Cynthia Forehand, Ph.D. Dean, Graduate College

Date: June 24, 2014

Abstract

The problem of the falling under gravity suspension droplet was examined for cases where the droplet contains particles with different densities and different sizes. Cases examined include droplets composed of uniform-size particles with two different densities, of uniform-density particles of two different sizes, and of a distribution of particles of different densities. The study was conducted using both simulations based on Oseenlet particle interactions and laboratory experiments. It is observed that when the particles in the suspension droplet have different sizes and densities, an interesting segregation phenomenon occurs in which lighter/smaller particles are transported downward with the droplet and preferentially leave the droplet by entering into the droplet tail, whereas heavier/larger particles remain for longer periods of time in the droplet. When computations are performed with two particle densities or two particle sizes, a point is eventually reached where all of the lighter/smaller particles have been ejected from the droplet, and the droplet continues to fall with only the heavier/larger particles. A simple model explaining three stages of this segregation process is presented.

Acknowledgments

I would first like to express great appreciation to my advisor, Dr. Jeffrey Marshall, who I would not have been able to complete this thesis without. It has been amazing to be able to work with a professor who takes the time to explain concepts to me, no matter how long it may take, and who truly cares that I do understand the subject at hand. I have been incredibly lucky to have had the opportunity to work with such a knowledgeable, helpful, patient, and passionate advisor, who has provided me with guidance throughout the entirety of my thesis work.

I would also like to thank the members of my thesis committee, Dr. Yves Dubief and Dr. Christopher Danforth, for their ideas, guidance, and the invaluable time they have spent working on my thesis committee.

I would like to express gratitude to my friends and classmates, who have provided support and comic relief throughout this process, and to my family, for their endless support both before and during my thesis work. I would not be where I am today without them.

Table of Contents

Acknowledgments.....	ii
List of Tables	iv
List of Figures.....	v
Chapter 1 Motivation and Objectives	1
1.1. Motivation.....	1
1.2. Objective and Scope	5
Chapter 2 Literature Review	7
2.1. Stokesian Dynamics and Oseen Dynamics.....	7
2.2. The Problem of a Falling Suspension Droplet.....	13
Chapter 3 Computational Method.....	31
3.1. Oseen Dynamics Simulation Method	31
3.2. Particle Motion.....	35
Chapter 4 Computational Results	39
4.1. Suspension Droplets with Uniform Particle Properties	40
4.2. Suspension Droplets with Variable Particle Density.....	47
4.3. Suspension Droplets with Variable Particle Size.....	57
4.4. Suspension Droplets with Size and Density Distributions	63
4.5. Mechanisms of Preferential Leakage of Light/Small Particles into the Droplet Tail	67
Chapter 5 Experimental Investigation	74
5.1. Experimental Method.....	74
5.2. Experimental Results	78
Chapter 6 Conclusions and Future Work.....	90
References.....	95

List of Tables

Table 1: Average dimensionless fall velocity of an isolated particle (non-dimensionalized by the fall velocity of the nominal particle U) for each of five bins in simulations in which particle size and density are set using a Gaussian random variable with standard deviation σ	64
Table 2: Characteristics of particles used in the experiments	76
Table 3: Parameters characterizing the experimental data sets.	78

List of Figures

Figure	Page
Figure 1: Time evolution of the falling suspension droplet for initial volume fraction $\phi = 0.02$. (a) $N = 160$, $\varepsilon = 0.05$, (b) $N = 320$, $\varepsilon = 0.0397$. (From Nitsche & Batchelor, 1997).	16
Figure 2: Experimental results showing tail formation. Where $d_p = 0.9mm$, $d_d = 7mm$, $Re_p = 10^{-3}$, and $Re_d = 0.25$. (From Nitsche & Batchelor, 1997).....	17
Figure 3: The breakup of suspension droplets at different Reynolds numbers with $\phi = 0.02$, $N = 756,000$. (A) is a top view and (B) is a side view (From Bosse et al., 2004).	19
Figure 4: Snapshots of a falling suspension droplet where (a) is a simulation with $N = 3,000$, and (b) is an experiment with $N = 950 - 1450$ (From Metzger et al., 2007).	21
Figure 5: The regimes of evolution for a falling suspension droplet as a function of the ratio of droplet radius to particle radius (R_0/a), the particle Reynolds number (Re_p), and the volume fraction ϕ . The dashed and dotted lines represent the transition from the Stokes cloud regime to the Macro-scale inertia regime for $\phi = 0.5$ and 0.05 respectively. The symbols are the following: *, experiments of Metzger et al. (2007) with $\phi = 0.04$ and $\phi = 0.2$; Δ and O are experiments at $\phi = 0.02 - 0.1$ and $\phi = 0.5$ respectively (From Pignatel et al., 2011).	22
Figure 6: Typical evolution of a falling suspension droplet in the micro-scale inertia regime where $l^* \approx 1$ and there is no significant particle leakage. (a) Oseenlet simulations	

with $N = 2000$ and $l^* = 1$, (b) experimental results with $N = 600$, $Re_d = 15$, and $l^* = 0.65$ (From Pignatel et al., 2011). 23

Figure 7: Typical evolution of a falling suspension droplet in the micro-scale inertia regime where $l^* \approx 20$ and there is significant particle leakage. (a) Oseenlet simulations with $N = 7500$ and $l^* = 20$, (b) experimental results with $N = 7000$, $Re_d = 3.5$, and $l^* = 21$ (From Pignatel et al., 2011). 24

Figure 8: Droplet fall velocity versus time for simulations with Δ , $N = 500$; \triangleright , $N = 5000$, for different l^* values and Stokeslet conditions (From Pignatel et al., 2011). 25

Figure 9: Streamlines of a droplet of pure liquid falling in an ambient fluid (From McHale et al.). 26

Figure 10: Streamlines of a suspension droplet falling in an ambient fluid, where the boundary of closed fluid streamlines is shifted a finite distance inside the boundary of the droplet due to the gravitational slip of the excess mass (From Nitsche & Batchelor, 1997). 27

Figure 11: The percentage of particles that have leaked out of the droplet versus time. The dashed and solid lines represent averaged numerical runs for $N = 500$ and $N = 2000$ respectively. Different shapes represent different experimental runs under the same conditions, where filled shapes are for $N \approx 500$ and open shapes are for $N \approx 2000$ (From Metzger et al., 2007). 28

Figure 12: (a) The average departure distance from the Hadamard-Rybczynski toroidal closed streamlines (D^*) versus time for different values of N , and (b) the rate of departure dD^*/dt^* versus N (From Metzger et al., 2007). 29

Figure 13: Experimental droplet Reynolds number (Re_c) versus the product of the initial number of particles in the droplet by the particle Reynolds number. The dashed line represents $Re_c = 6N_0 Re_p / 5$, and the symbols are the same as those in Figure 5 (From Pignatel et al., 2011). 30

Figure 14: Schematic diagram illustrating the different regions in the velocity field induced around a spherical particle with radius r_p traveling with velocity v , according to the solution of the Oseen equations., drawn in a frame traveling with the particle. The velocity field reduces to the Stokes flow solution near the particle. In the far field, it has the form of a potential source, with $O(1/r^2)$ decay, and a thin wake region, with $O(1/r)$ decay. The transition region between the near and far fields occurs at a distance equal to the inertial screen length $\ell = r_p / \text{Re}_p$ away from the particle..... 33

Figure 15: Comparison of the dimensionless velocity magnitude as a function of distance for a stokeslet plus a potential doublet (dashed line) and for the oseenlet solution (solid line) along a ray starting from the sphere centroid, with angles (a) $\theta = 0$, (b) $\pi/4$, (c) $\pi/2$, and (d) π . The computations are for a case with particle Reynolds number $\text{Re}_p = 0.1$.. 34

Figure 16: Plot showing formation of tail behind a falling suspension droplet for a computation with a uniform particle type and $\text{Re}_d = 10$. Images are shown at times (a) $t^* = 0$, (b) 0.6, (c) 0.8, (d) 1.0 and (e) 1.2. 42

Figure 17: Contour plot of fluid velocity magnitude within a falling suspension droplet, with superimposed fluid streamlines and particles, at time $t^* = 4.5$ for the case of uniform particles. 43

Figure 18: Plot showing the time variation of the (a) average y -position and (b) fall velocity for a droplet of uniform size particles at different droplet Reynolds numbers. .. 44

Figure 19: Time variation of (a) the percentage of particles that remain in the droplet and (b) the computed average fall velocity divided by the solution (2.9). The plots are for uniform droplet size and different droplet Reynolds numbers, and the color legend is the same as used in Figure 18. 45

Figure 20: Plot showing the time variation of the root-mean-square y -position and the value of $(y_{\max}^* - y_{\min}^*)/4$ for a droplet of uniform size particles at different droplet Reynolds numbers. The color legend is the same as used in Figure 18..... 46

Figure 21: Time series of a droplet with $N = 50$, for a case with particles of two densities where $\beta = 0.5$. Images are shown at times (a) $t^* = 0$, (b) 0.6, (c) 1.0, (d) 1.4 and (e) 1.8. The light particles are shown in blue and the heavy particles in red. 49

Figure 22: Time series of a droplet with $N = 300$, showing preferential leakage of lighter particles into the droplet tail, for a case with particles with two densities with $\beta = 0.5$. Images are shown at times (a) $t^* = 0$, (b) 0.2, (c) 0.4, (d) 0.6 and (e) 1.0. The light particles are shown in blue and the heavy particles in red..... 50

Figure 23: (a) Comparison of the average fall velocity of the heavy particles (dark lines) and the light particles (dashed lines) plotted with time for varying β . (b) Comparison of the droplet fall velocity for varying β plotted with time. $\beta = 0$ (pink line), 0.25 (red lines), 0.5 (blue lines), 0.65 (green lines), and 0.75 (black lines)..... 52

Figure 24: Plot of (a) y_{rms} and (b) percentage of particles P remaining in the droplet as a functions of time with different values of β , comparing values for the heavy particles (solid lines) and for the light particles (dashed lines). The plot uses the same legend as in Figure 23. 53

Figure 25: Plot showing time variation of the mixing index G_{light} time for $\beta = 0.05$ (pink curve), $\beta = 0.1$ (orange curve), $\beta = 0.25$ (red curve), $\beta = 0.5$ (blue curve), $\beta = 0.65$ (green curve), and $\beta = 0.75$ (black curve). 57

Figure 26: Time series of a falling droplet for a case with two particles sizes with $\alpha = 0.41$, so that $d_1 / L = 0.1$ (red) and $d_2 / L = 0.026$ (blue), showing preferential motion of the small particles into the tail. Images are shown at times (a) $t^* = 0$, (b) 0.2, (c) 0.4, (d) 0.6 and (e) 0.8. 58

Figure 27: Comparison of the (a) average fall velocity and (b) droplet fall velocity as functions of t^* for $\alpha = 0$ (pink line), 0.14 (red lines), 0.22 (blue lines), 0.41 (green lines), and 0.57 (black lines). In (a), the large particles are indicated using dark lines and the small particles are indicated using dashed lines. 60

Figure 28: Plot of (a) y_{rms} and (b) percentage of particles P remaining in the droplet as a functions of time with different values of α , comparing values for the large particles

(solid lines) and for the small particles (dashed lines). The plot uses the same legend as in Figure 27.	61
Figure 29: Plot showing time variation of the mixing index G_{small} for $\alpha = 0.14$ (red line), 0.22 (blue line), 0.41 (green line), and 0.57 (black line).	62
Figure 30: Time variation of (a) y_{ave}^* and (b) $v_{ave}^* = -dy_{ave}^* / dt^*$ for five different bins in a simulation with a distribution of particle size and density having standard deviation $\sigma = 0.4$. Figure (b) uses the same legend as in (a).	65
Figure 31: Time variation of (a) y_{rms}^* and (b) percentage of particles within the bin remaining in the droplet for five different bins in a simulation with a distribution of particle size and density having standard deviation $\sigma = 0.4$. The plots use the same legend as in Figure 30a.	65
Figure 32: Plot showing a scatter diagram of the droplet and the near section of the tail for the case with distributed particle size and density with $\sigma = 0.4$, at times (a) $t = 1$, (b) 2, (c) 4, and (d) 5. The scatter size shown is proportional to the particle diameter, and the particle density is indicated by color as given by the legend on the right (in kg/m^3).	67
Figure 33: Plot showing particle locations for a computation with two densities and $\beta = 0.5$, showing times characteristic of tail formation stages: (a) Stage 1 ($t^* = 0.6$), (b) Stage 2 ($t^* = 3.0$), (c) Stage 3 ($t^* = 10.0$).	69
Figure 34: Schematic diagram showing fluid streamlines (on the left) and particle pathlines (on the right) in a frame moving with the suspension droplet. Due to downward particle slip relative to the fluid, the fluid streamlines penetrate the outer part of the droplet giving an effective droplet boundary (dashed line on the left) that has smaller radius than the droplet. Particles in Region I are within the no-penetration surface so the fluid flow is always in the direction of particle motion, whereas particles in Region II (shaded grey) experience fluid flow counter to the direction of particle motion when they pass through the tail formation region (indicated by a dashed circle). Region III denotes the exterior of the droplet.	71

Figure 35: Diagram of the experimental set-up including (A) the black background, (B) the injection syringe, (C) the lighting system, (D) the video camera, (E) the ruler, and (F) the vessel..... 75

Figure 36: Photo of the particle positions of a falling droplet, with initial droplet diameter $d_d = 3.8$ mm, in experimental set 1 at times (seconds): (a) $t = 0$, (b) $t = 0.8$, (c) $t = 1.8$, (d) $t = 3.8$, and (e) $t = 4.3$. The large particles (red) are about 2.2 times larger than the small particles (gold)..... 81

Figure 37: Photo of the particle positions of a falling droplet with initial droplet diameter $d_d = 4$ mm in experimental set 2 at times (seconds): (a) $t = 0$, (b) $t = 1.2$, (c) $t = 2.7$, and (d) $t = 4.2$. The heavy particles (silver) are 14% heavier than the light particles (red). 82

Figure 38: Photo of the particle positions of a falling droplet with initial; droplet diameter initial $d_d = 3.5$ mm in experimental set 3 at times (seconds): (a) $t = 0$, (b) $t = 0.44$, (c) $t = 0.94$, (d) $t = 1.4$, and (e) $t = 1.74$. The large/heavy particles (silver) are 27% larger and 3.2 times heavier than the small/light particles (red). 82

Figure 39: Experimental droplet fall velocity versus time: (a) experimental set 1 (triangles), (b) set 2 (circles), (c) set 3 (squares). 84

Figure 40: Plots showing the percentage of each type of particle contained in the vertical tail with time, out of the total number of each type of particle for (a) experimental set 1, (b) set 2, and (c) set 3. Solid lines represent heavier (or larger) particles and dashed lines represent lighter (or smaller) particles. 86

Figure 41: Experimental droplet fall velocity divided by solution to (2.9) plotted with time. (a) experimental set 1, (b) experimental set 2, (c) experimental set 3. 89

Chapter 1

Motivation and Objectives

1.1. Motivation

A *suspension droplet* is a particulate flow generated by an initial 'droplet' formed of a particulate suspension which is placed in a liquid that has no particles outside of the droplet. When the particle density is different from that of the surrounding liquid, the suspension droplet either falls or rises (for heavier or lighter particles, respectively) in the presence of a gravitational field. The problem of a falling suspension droplet containing particles of varying characteristics is of interest for three very different reasons: (1) the problem is a highly simplified representation of a number of important applications involving dynamics of particle clusters moving relative to the surrounding fluid, (2) the problem offers the opportunity to solve for particle hydrodynamic interaction using a relatively new computational method – which we call *Oseen dynamics* – that has a great deal of potential for accounting for particle interactions in discrete element methods, and (3) the problem addresses fundamental issues of how particle hydrodynamic interactions influence segregation of particles with different sizes and densities in a two-phase fluid.

The dynamics of a falling suspension droplet, and segregation of particles of different characteristics within the droplet, are important aspects of a number of applications involving motion of clusters in particle flow, particularly in the presence of gravity or other body forces. This problem is relevant to a number of geophysical and environmental applications in which clusters of heavy particles generate turbulence as they sink in a lighter fluid, as well as applications in which plumes of light particles rise in a heavier fluid (Hurley and Physick, 1993). In direct numerical simulations of homogeneous turbulence of a particulate fluid under gravity, Elgobashi and Truesdell (1993) observed that the falling particle clusters in the gravitational field was the primary mechanism for turbulence generation within the flow. The dynamics of a falling suspension droplet are also important in problems of smoke inhalation in the human lung. It has been observed by a number of investigators (Martonen, 1992; Phalen et al., 1994; Robinson and Yu, 2001) that in cases with high particle concentrations, the deposition of particles in inhaled cigarette smoke is much greater than predicted values based on single-particle settling velocities. One reason that has been proposed to explain this difference is that smoke particles move through the upper airway region in the form of a suspension cloud. The hydrodynamic interaction of particles within this suspension cloud allow the particles to travel more rapidly relative to the surrounding fluid than would be the case for isolated particles, allowing the particles to penetrate further into the lung than would be possible for isolated particles. Understanding where the different types of particles settle due to segregation is very important in understanding the health effects of

breathing in cigarette smoke, as well as related problems of inhalable drug dispersal and dust inhalation in construction environments.

When developing computational models for a fluid flow containing particles, it is often important not only to capture the effects of the fluid on the particles, but to also simulate the effects of the particles on the fluid. It is often the case that particulate flows contain far too many particles to solve for the fluid flow on a fine grid placed about each particle, so the standard method for dealing with particle interaction with the flow is to impose an additional body force on the fluid that represents an average of the particle-induced force over some region that is large compared to the particle dimensions. While this method is effective at predicting bulk interactions between the particles and the fluid, it is not sufficiently refined to predict hydrodynamic interactions between individual particles on the scale of a particle cluster. These local particle hydrodynamic interactions can significantly influence the dynamics of a flow field. For instance, in the case of a falling suspension droplet, these local particle hydrodynamic interactions cause the suspension droplet to fall significantly more rapidly than it would fall with non-interacting particles. This difference between the individual particle settling velocity and the settling velocity of the suspension droplet is a driving force behind the segregation of particles with different properties that are initially randomly distributed within a suspension droplet. The *Stokesian dynamics* method takes into account the local particle hydrodynamic interactions by modeling each particle as a stokeslet and a potential doublet, allowing for these important properties to be accounted for without the need for computing for the flow on a grid about each particle. Unfortunately, the Stokesian

dynamics method is of limited applicability for many flows because it requires the Reynolds number for the entire flow to be small compared to unity. To overcome this restriction, Oseen dynamics uses the full Oseen solution for flow past a particle in an unbounded domain. This method still requires that the particle Reynolds number is small compared to unity, although it removes the restriction that the Reynolds number of the entire flow must be small. Since the problem of a falling suspension droplet is both highly dependent on particle hydrodynamic interactions and since this flow occurs in an unbounded domain, it is a useful example problem with which to explore and test the Oseen dynamics approach for particle hydrodynamic simulations.

It is often observed in particulate flows composed of particles of different sizes or densities that particles of similar characteristics seem to separate from the bulk flow. This phenomenon, called *segregation*, acts in opposition to the related phenomenon of particle mixing, and the resulting particle distribution is determined by a balance between these two effects. Most studies of particle segregation have been performed for granular flows (Jain et al., 2005; Li and McCarthy, 2003), in which particle motion is determined only by collision and adhesion forces from other particles. Studies of segregation of particle mixtures with an interstitial fluid have found that the rate and amount of segregation is strongly influenced by the fluid flow. Roeder et al. (1995) observe that segregation of particle mixtures in a centrifugal flow is significantly inhibited by the particle hydrodynamic interactions, and they propose that the particle drafting phenomenon is responsible for suppressing separation of particles with different characteristics. On the other hand, a flow field can also be the cause of particle segregation. For instance, the

phenomenon of margination in blood flow occurs when the different components of blood (RBCs, leukocytes, platelets, etc.) become radially segregated in the presence of a channel flow (Aarts et al., 1988; Kumar and Graham, 2012). In this latter case, the shear-induced migration phenomenon discussed by Leighton and Acrivos (1987) provides a driving force for radial segregation in the channel flow, whereas in the case of gravitational or centrifugal segregation the driving force for segregation is externally imposed via a body force. The problem of a falling suspension droplet formed of a particle mixture with a distribution of particle sizes and densities provides relatively simple problem with which to examine the effects of particle hydrodynamic interaction of the segregation phenomenon for a case with imposed driving force (gravity).

1.2. Objective and Scope

The overall objective of this study is to gain a better understanding of how local particle hydrodynamic interactions and the segregation of particles are related for a problem in which segregation is driven by an externally imposed body force (gravity). The study seeks to understand and explain the details of particle segregation for cases with different particle and flow conditions where the inertial effects of the flow are important. The specific flow that we have used to examine this problem is that of a particulate suspension droplet falling under gravity in an unbounded fluid. This problem is studied computationally, using a combination of the discrete element method and Oseen dynamics, as well as experimentally. Cases are examined with bimodal mixtures with two particles densities and with two particle sizes, as well as problems with broad

distributions of particle density and size. Specific features of the problem examined include the ability of particle hydrodynamic interactions to inhibit separation of a falling droplet with sufficiently high particle concentration, and the fluid mechanics governing particle segregation into the tail of a suspension droplet. The study is also one of only two investigations that have been performed to date using the Oseen dynamics approach, and so a secondary objective of this work is to explore and better understand this computational method.

Chapter 2

Literature Review

2.1. Stokesian Dynamics and Oseen Dynamics

As particles move relative to a fluid, forces and torques are not only induced on the particle by the flow, but also on the flow from the particles. If the flow is densely filled with particles, the forces and torques exerted on the flow by the particles can significantly influence the dynamics of the flow. Stokesian dynamics is an approach that is used to simulate many particles that are dispersed or suspended in a fluid and takes into account the hydrodynamic forces induced on the particle by the flow, and on the flow from the particle. An overview of the basic theory of Stokesian dynamics is given in the review article by Brady and Bossis (1988), and is summarized below.

The velocity induced by a stress distribution $\mathbf{t}(\mathbf{x})$ defined on the surface S of the particle, at a point \mathbf{x} located outside of the particle is given for a Stokes flow by

$$u_i(\mathbf{x}) = -\frac{1}{8\pi\mu} \int_S G_{ij}(\mathbf{x}, \mathbf{x}') t_j(\mathbf{x}') da' . \quad (2.1)$$

Where μ is the dynamic viscosity of the fluid and the components of the velocity vector \mathbf{u} , the stress vector \mathbf{t} , and the second-order tensor \mathbf{G} , are represented in (2.1) through the use of tensor indices. The stress vector for a Newtonian fluid is equal to

$$\mathbf{t} = -p\mathbf{n} + 2\mu\mathbf{D} \cdot \mathbf{n}, \quad (2.2)$$

where p is pressure, \mathbf{n} is the unit normal vector of S , and \mathbf{D} is the rate of deformation tensor, which is equal to the symmetric portion of the velocity gradient tensor. The tensor \mathbf{G} is defined using the Oseen tensor $\mathbf{W}(\mathbf{x}, \mathbf{x}')$ as $G_{ij} = 8\pi\mu W_{ij}$, where the Oseen tensor is defined as

$$\mathbf{W}(\mathbf{x}, \mathbf{x}') = \frac{1}{8\pi\mu} \left[\frac{\mathbf{I}}{r} + \frac{(\mathbf{x} - \mathbf{x}')(\mathbf{x} - \mathbf{x}')^T}{r^3} \right], \quad (2.3)$$

and $r \equiv |\mathbf{x} - \mathbf{x}'|$ is the distance between points \mathbf{x} and \mathbf{x}' , and \mathbf{I} is the identity tensor.

The main concept of the Stokesian dynamics method is to write the fluid velocity at a point \mathbf{x} as (Pozrikidis, 1992)

$$u_i(\mathbf{x}) = -\frac{1}{8\pi\mu} \left[G_{ij}(\mathbf{x}, \xi) \int_S t_j(\mathbf{x}') da' + \frac{\partial G_{ij}}{\partial \xi_k}(\mathbf{x}, \xi) \int_S (x'_k - \xi_k) t_j(x') da' + \dots \right]. \quad (2.4)$$

This equation is a multipole expansion of the integral in (2.1) about the centroid of the particle ξ . This expansion is usually truncated after the first two terms because it is generally only used for points that are located a significant distance away from the particle. The first term in (2.4), which is often called the stokeslet or point force, is the total force exerted on the particle. The second term in (2.4) is the flow resulting from a force doublet. The doublet can be decomposed into a symmetric part that is written in

terms of a stresslet, and an anti-symmetric part that is written in terms of a rotlet (or a point torque). The velocity equation written in the form of (2.4) is advantageous because the integrals are not dependent on the position of the point \mathbf{x} (where it is desired for the velocity calculated), and are only dependent on the location relative to the centroid position on the particle surface and on the stress. This allows for the integrals to only be solved once each time step and used to find the velocity at any point in the flow field at that time step.

Nitsche and Batchelor (1997) used this method to study the dynamics of a cluster of particles falling in a stationary fluid. To perform these simulations, the particles were set to travel at their terminal velocity by balancing drag force on each particle with the gravitational force. The relative velocity between a particle and the fluid was then defined as

$$\mathbf{v} - \mathbf{u} = -\frac{mg_R}{3\pi\mu d_p} \mathbf{e}_z, \quad (2.5)$$

where \mathbf{v} is the particle velocity, \mathbf{u} is the fluid velocity, g_R is the reduced gravitational acceleration, d_p is the particle diameter, and m is the mass of the particle. The induced velocity by the other particles on the fluid velocity was accounted for setting the fluid velocity at any point \mathbf{x} in the flow field equal to the sum of the velocity induced by the different particles, defining the fluid velocity \mathbf{u}_i evaluated at the centroid of particle i as

$$\mathbf{u}_i = \sum_{j \neq i} \mathbf{W}(\mathbf{x}_i, \mathbf{x}_j) \cdot \mathbf{F}_{d,j}, \quad (2.6)$$

where $\mathbf{F}_{d,j}$ is the Stokes drag force on particle j . Results of this study are discussed in the next section.

One problem that is often encountered in Stokesian dynamics calculations results from the method not accounting for contact forces between the particles. Because these contact forces are not accounted for in the computations, particles can sometimes come close to each other, which causes the computations to break down quickly, resulting from singularities at the particle centroid. To solve this problem, Cortez (2001), (along with others, eg. Krasny (1986) and Cortez and Varela (1997)) distributes a force over a finite region in order to develop nonsingular versions of the stokeslet. Other methods have also been used to avoid this problem. Nitsche and Batchelor (1997) introduced a short range repulsive force in their computations, Machu et al. introduced a cutoff length, and others such as Metzger et al. (2001), who studied a falling droplet of particles, simply only did computations where this issue would not arise; in their case this meant avoiding clouds consisting of a small number of particles where the velocity of the pair of particles would often exceed the velocity of the droplet. Another way that this problem can be avoided when using Stokesian dynamics is to use a DEM approach to model the particle interactions along with the Stokesian dynamics method. A DEM approach avoids the issue of particles becoming too close together because it uses contact forces that keep the particles a sufficient distance away from each other.

Another factor that can greatly complicate the Stokesian dynamics method is the presence of macroscale surfaces in the flow. Blake (1971) and Bossis et al. (1991) show that analytical terms can be used to represent the image of the stokeslet over the wall for

very simple flow geometries. This becomes difficult though once geometries become more complicated than geometries such as a sphere or a flat surface. Pozrikidis (1992) shows that the Stokes flow can be computed in flow geometries that are more complicated through the use of a boundary element method. A new set of problems can be encountered while using this method though. If a particle is small enough compared to the size of the flow discretization panels, then resolving the particle image set when it is close to the wall can become very problematic.

Another requirement of the Stokesian dynamics method is that a matrix equation needs to be solved for the fluid velocity at the centroid of each particle. To directly solve this matrix for a system containing N particles, $O(N^3)$ calculations per time step are required. Even when a more efficient iterative matrix solver is used, $O(N^2)$ calculations are still required. Sierou and Brady (2001) address this computational issue by giving a faster matrix solution approach that uses Fourier transforms and improves the computations by requiring only $O(N \ln N)$ computations per time step.

One of the main limitations of the Stokesian dynamics method is that it requires that the Reynolds number for the entire flow, i.e. the droplet Reynolds number Re_d , be small compared to unity throughout the flow. The reason for this restriction is that the Stokes solution is only valid within distances that are small compared to the inertial screening length $\ell = r_p / Re_p$ of the particle centroid, where Re_p is the particle Reynolds number, and r_p is the particle radius. Lomholt and Maxey (2003) use a force coupling method that first distributes the particle force to a grid and then uses the full form of the Navier-Stokes equation to solve for the flow field on the grid. This method helps to

remove the small Reynolds number requirement, although it takes much more time than the Stokesian dynamics method. Subramanian and Koch (2008) address this problem by using *Oseen dynamics* to study the problem of a falling droplet of particles. In this case, this method is valid for arbitrary flow Reynolds numbers, and only requires that the particle Reynolds numbers is small. The *Oseen dynamics* method is very similar to the Stokesian dynamics method that is used by Nitsche and Batchelor (1997), except is uses the full Oseen solution for hydrodynamic interaction of the particles (Proudman and Pearson, 1957).

2.2. The Problem of a Falling Suspension Droplet

Interest in the problem of a falling under gravity suspension droplet in the fluid mechanics community has led to some commonly defined problem parameters. A particle Reynolds number ($\text{Re}_p = 2r_p U / \nu$) and a droplet Reynolds number ($\text{Re}_d = 2r_d U_{d,HR} / \nu$) are often used to describe suspension droplets, where r_p is the particle radius, r_d is the droplet radius, U is the settling velocity of an isolated particle, $U_{d,HR}$ is a theoretical estimate of the droplet settling velocity based on the initial number of particles in the droplet, and ν is the kinematic viscosity of the suspending fluid. A simple theoretical expression for droplet fall velocity is often studied in the literature and is obtained by treating the particle suspension as a droplet of another (immiscible) fluid with effective density ρ_d and viscosity μ_d , in a fluid with effective density ρ_f and viscosity μ_f . The solution for drag on a fluid droplet suspended in an immiscible liquid was given independently by Hadamard (1911) and Rybczynski (1911) as

$$U_{d,HR} = \frac{(\rho_d - \rho_f)gL^2}{12\mu_f} \left(\frac{\mu_f + \mu_d}{\mu_f + \frac{3}{2}\mu_d} \right) \quad (2.7)$$

The density difference in (2.7) can be written in terms of the particle volume concentration $\phi = N\varepsilon^3$ within the droplet as $\rho_d - \rho_f = \phi(\rho_p - \rho_f)$, where N is the number of particles in the droplet, and ε is the non-dimensionalized particle diameter,

$\varepsilon = \frac{d_p}{d_d}$. The effective viscosity is given for small concentrations by the Einstein expression

$$\mu_d = \mu_f \left(1 + \frac{5}{2} \phi\right). \quad (2.8)$$

Linearizing (2.7) for small concentration values and dividing by the isolated particle fall velocity U_p yields

$$U_{d,HR}^* \equiv \frac{U_{d,HR}}{U} = \frac{6}{5} N \varepsilon. \quad (2.9)$$

Here U_d denotes the fall velocity only of the N particles contained within the droplet, and does not include the particles in the tail.

The dynamics of a suspension droplet falling under gravity have been studied computationally and experimentally for cases where both the Re_p and the Re_d are small. The settling of an initially spherical particle suspension droplet under gravity was examined by Nitsche and Batchelor (1997) using both experiments and a Stokesian dynamics simulation approach for low Reynolds-number clouds, based on modeling each particle by a stokeslet and a doublet that induce a velocity field on all other particles. Machu et al. (2001), Metzger et al. (2007), and Ekiel-Jezewska et al. (2006b) all used similar Stokesian dynamics methods to study the behavior of a suspension droplet of spherical particles falling under gravity, and Park et al. (2010) also used a similar method to study the behavior of a suspension droplet of rigid fibers falling under gravity.

Other computations and experiments study the dynamics of a falling under gravity suspension droplets for cases where the Re_p is small and the Re_d is anywhere from

small to moderate. Bosse et al (2005) approximated the fluid-particle interaction force as a distributed body force on a grid, from which they solved for the induced flow field using a pseudo-spectral technique. Chen and Marshall (1999) employed a vorticity-based method in which the curl of the fluid-particle interaction force acts as a source term in the vorticity transport equation. The solution was obtained (in two dimensions) using an entirely Lagrangian approach that employed a combination of vortex blobs and point particles. A similar method was employed in three dimensions by Walter and Koumoutsakos (2001), in which a vortex-in-cell method was used to compute the velocity field. Subramanian and Koch (2008) noted that if the particle Reynolds number $Re_p = 2r_p |\mathbf{u} - \mathbf{v}| / \nu$ is small compared to unity, where r_p is the particle radius, \mathbf{v} is the particle velocity, and \mathbf{u} is the fluid velocity at the particle centroid, and the cloud Reynolds number is not small, then the Stokesian dynamics approach can be extended using the full Oseen solution for particle interactions, where the oseenlet replaces the stokeslet and the potential doublet in the Stokesian dynamics approach. This method was also used by Pignatelli et al. (2011), along with experiments, to explore suspension droplet dynamics at finite droplet Reynolds numbers.

Properties of the suspension droplet were studied as the droplet evolved with time for many different cases. Nitsche and Batchelor (1997) performed computations for blobs typically containing $N = 80, 160, \text{ or } 320$ particles with an initial particle volume fraction of 4% or less. As shown in Figure 1, these computations showed that the suspension droplet slowly loses particles by shedding them erratically along the vertical axis from the rear of the droplet.

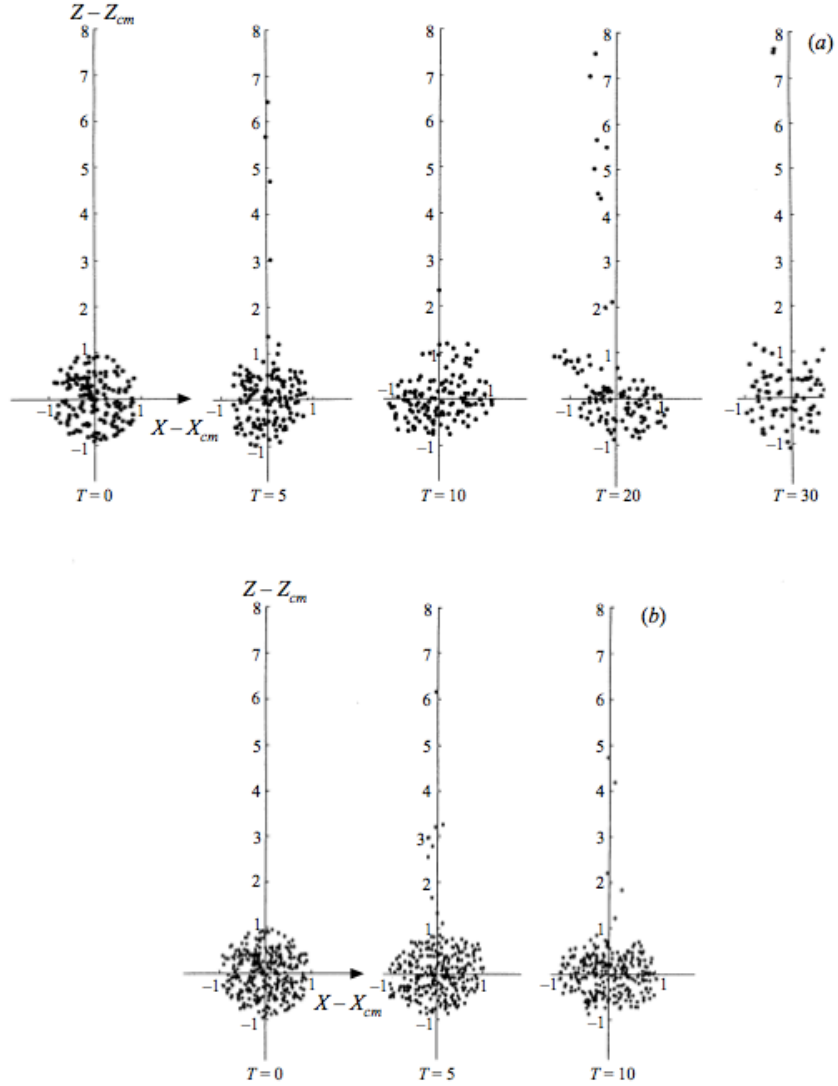


Figure 1: Time evolution of the falling suspension droplet for initial volume fraction $\phi = 0.02$. (a) $N = 160$, $\varepsilon = 0.05$, (b) $N = 320$, $\varepsilon = 0.0397$. (From Nitsche & Batchelor, 1997).

In addition, the particles that remain in the droplet are evenly distributed throughout the droplet, and the droplet remains approximately spherical in shape with a diameter that is roughly constant at its initial value. This behavior was also seen by Machu et al. (2001), Bosse et al. (2005), and Metzger et al. (2007). Nitsche and Batchelor (1997) also performed experiments consisting of particles with diameters of 0.9mm and $Re_p = 10^{-3}$

and droplets with diameters of 7mm and $Re_d = 0.25$. The blobs were more concentrated than in the computations, although they similarly remained approximately spherical and sporadically shed particles into the tail as well, as shown in Figure 2.

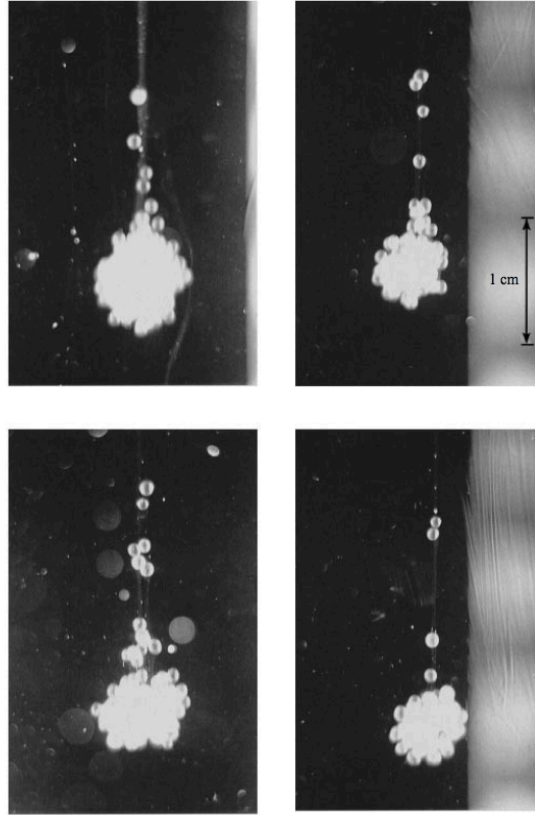


Figure 2: Experimental results showing tail formation. Where $d_p = 0.9mm$, $d_d = 7mm$, $Re_p = 10^{-3}$, and $Re_d = 0.25$. (From Nitsche & Batchelor, 1997).

As the suspension droplet falls downward, a series of transitions in the flow pattern take place after longer amounts of time (Adachi et al., 1978; Noh and Fernando, 1993). As originally described by Adachi et al (1978), the particle cloud in certain cases adopts a toroidal shape which breaks up into some number of offspring droplets, which then repeat the process. The evolution of a suspension droplet into a toroidal shape is analogous to a similar process that occurs for a droplet of a heavy liquid immersed in a

lighter liquid (Kojima et al., 1984). Bosse et al. (2004) did computations with droplet Reynolds numbers in the range of $1 \leq Re_d \leq 100$ and found that in this range the suspension droplet becomes a torus, eventually becomes unstable, and breaks up into a number of secondary drops, where the number of secondary drops increases with Re_d , these results are shown in Figure 3. Pignatelli et al. (2011) also conducted computations and experiments with similar parameters and observed a similar qualitative evolution. In this study by Bosse et al. (2004), a similar volume concentration ($\phi = N\epsilon^3$) to that used in Nitsche and Batchelor (1997) is used, although a larger amount of particles is used. The authors found that the number of secondary droplets is highly dependent on the number and size of particles, where cases with fewer, larger particles form fewer secondary drops and the torus breaks up sooner compared to cases with more plentiful, smaller particles. Metzger et al. (2007) performed computations and experiments for low Reynolds number flows and found that two scenarios for the droplet evolution with time typically arise, depending on the initial number of particles in the droplet. They found that clouds with $N \leq 500$ ($\phi = 0.04$) typically behave as Nitsche and Batchelor (1997) observed, where the cloud slowly loses particles from its rear forming a vertical tail, and the droplet retains its spherical shape until it is dispersed due to the depletion of particles in the blob.

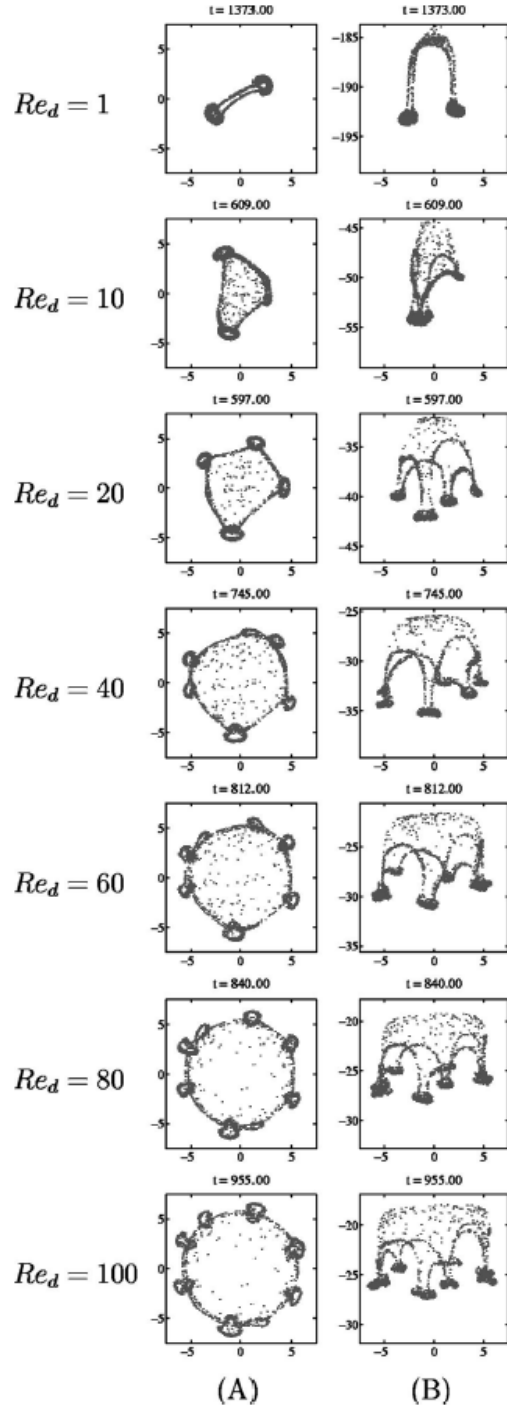


Figure 3: The breakup of suspension droplets at different Reynolds numbers with $\phi = 0.02$, $N = 756,000$. (A) is a top view and (B) is a side view (From Bosse et al., 2004).

The other scenario that the authors observed was for suspension droplets with $N \geq 500$ ($\phi = 0.2$). In this scenario, the droplet first slowly loses particles from the rear of the cloud forming a vertical tail; eventually the shape of the droplet flattens from a sphere to an oblate shape and forms a torus, which eventually breaks up into two droplets. If there are enough particles remaining in the two droplets, they can each form a torus that then will break up into two droplets, and the process can repeat depending on the number of particles remaining in the droplets. This process is shown for computations with $N = 3000$ and for experiments with $N > 1000$ in Figure 4.

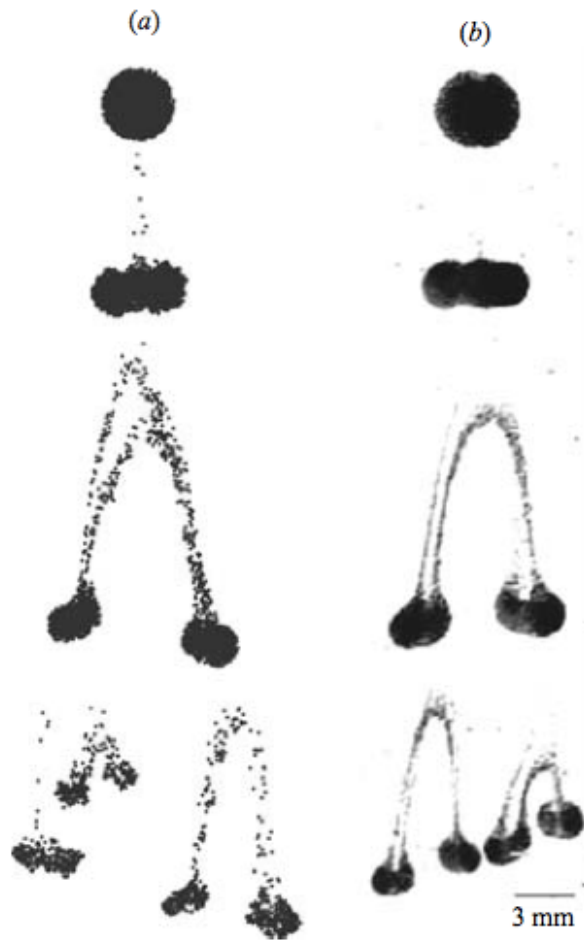


Figure 4: Snapshots of a falling suspension droplet where (a) is a simulation with $N = 3,000$, and (b) is an experiment with $N = 950 - 1450$ (From Metzger et al., 2007).

Subramanian and Koch (2008) present three regimes of evolution for a falling suspension droplet along with the transition points between each regime. The first regime presented is the ‘Stokes suspension drop’ regime, where both Re_p and Re_d are very small (inertial effects are negligible). The ‘Stokes suspension drop’ regime transfers into the next regime, the ‘macro-scale inertia’ regime, when inertia is increased. The transition occurs when $Re_d = 1$. A second transition into the ‘micro-scale inertia’ or ‘Oseen interactions dominated’ regime occurs when the inertial screening length

($l = r_p / Re_p$) is of the order of the cloud radius (ie. $r_d \sim r_p / Re_p$). Subramanian and Koch (2008) presented the different regimes in a graph, and Pignatel et al. (2011) adapted this graph slightly and the adapted graph is shown in Figure 5.

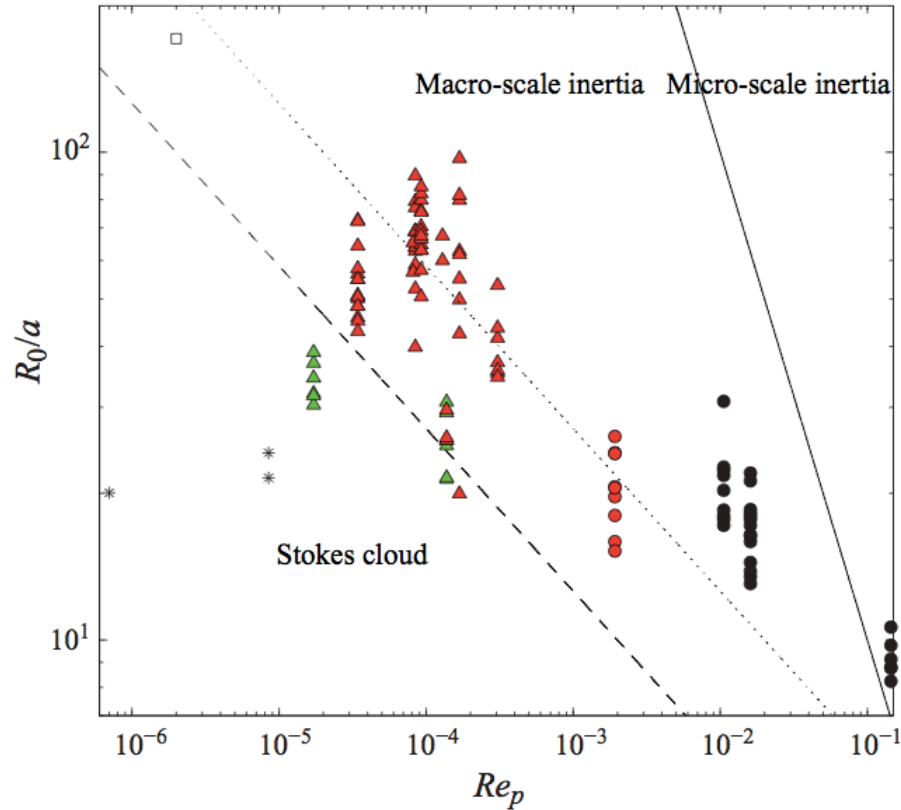


Figure 5: The regimes of evolution for a falling suspension droplet as a function of the ratio of droplet radius to particle radius (R_0/a), the particle Reynolds number (Re_p), and the volume fraction ϕ . The dashed and dotted lines represent the transition from the Stokes cloud regime to the Macro-scale inertia regime for $\phi = 0.5$ and 0.05 respectively. The symbols are the following: *, experiments of Metzger et al. (2007) with $\phi = 0.04$ and $\phi = 0.2$; Δ and O are experiments at $\phi = 0.02 - 0.1$ and $\phi = 0.5$ respectively (From Pignatel et al., 2011).

Pignatel et al. (2011) use both experiments and the Oseenlet simulations introduced by Subramanian and Koch (2008) to study the dynamics of a falling suspension droplet in the regimes where macro-scale inertia and micro-scale inertia are

dominant. In the macro-scale region, the experimental results were similar to those of Bosse et al. (2005). In this region the droplet eventually formed a torus and broke up into two separate blobs, with no significant particle leakage into the vertical tail. Simulations and experiments in the ‘micro-scale inertia’ regime showed that when the inertial screening length is of the order of the droplet size, ($l^* = (r_p/r_d)/\text{Re}_p$), the droplet behaves similarly to the case of ‘macro-scale inertial’ and also has no significant particle leakage. The experimental and computational results are shown for the case of $l^* \approx 1$ in Figure 6.

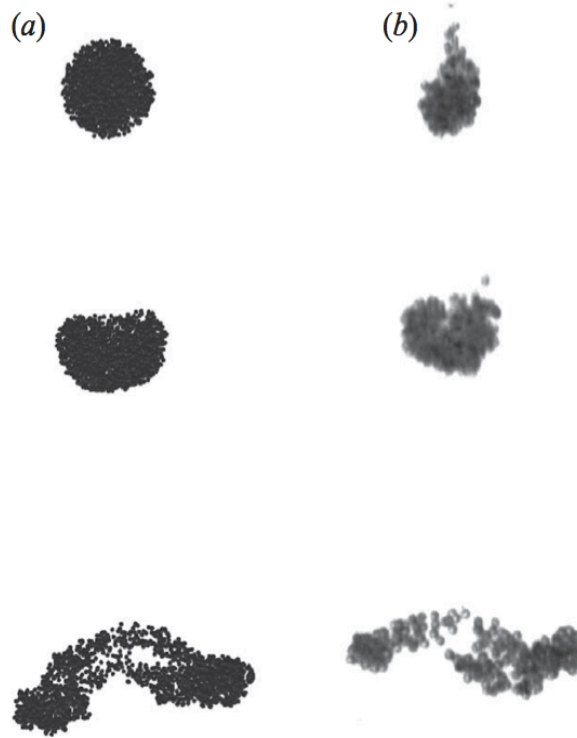


Figure 6: Typical evolution of a falling suspension droplet in the micro-scale inertia regime where $l^* \approx 1$ and there is no significant particle leakage. (a) Oseenlet simulations with $N = 2000$ and $l^* = 1$, (b) experimental results with $N = 600$, $\text{Re}_d = 15$, and $l^* = 0.65$ (From Pignatel et al., 2011).

Contrarily, when the inertial screening length is increased in the ‘micro-scale inertial’ regime, particle leakage is observed, and the droplet behaves similarly to a droplet in the ‘Stokes suspension droplet’ regime. Figure 7 shows the experimental and computational results for this case with $l^* \approx 20$. This is also quantitatively shown in Figure 8, which plots of the droplet fall velocity versus time for different values of l^* are compared with the droplet fall velocity versus time in the ‘Stokes suspension droplet’ regime.



Figure 7: Typical evolution of a falling suspension droplet in the micro-scale inertia regime where $l^* \approx 20$ and there is significant particle leakage. (a) Oseenlet simulations with $N = 7500$ and $l^* = 20$, (b) experimental results with $N = 7000$, $Re_d = 3.5$, and $l^* = 21$ (From Pignatel et al., 2011).

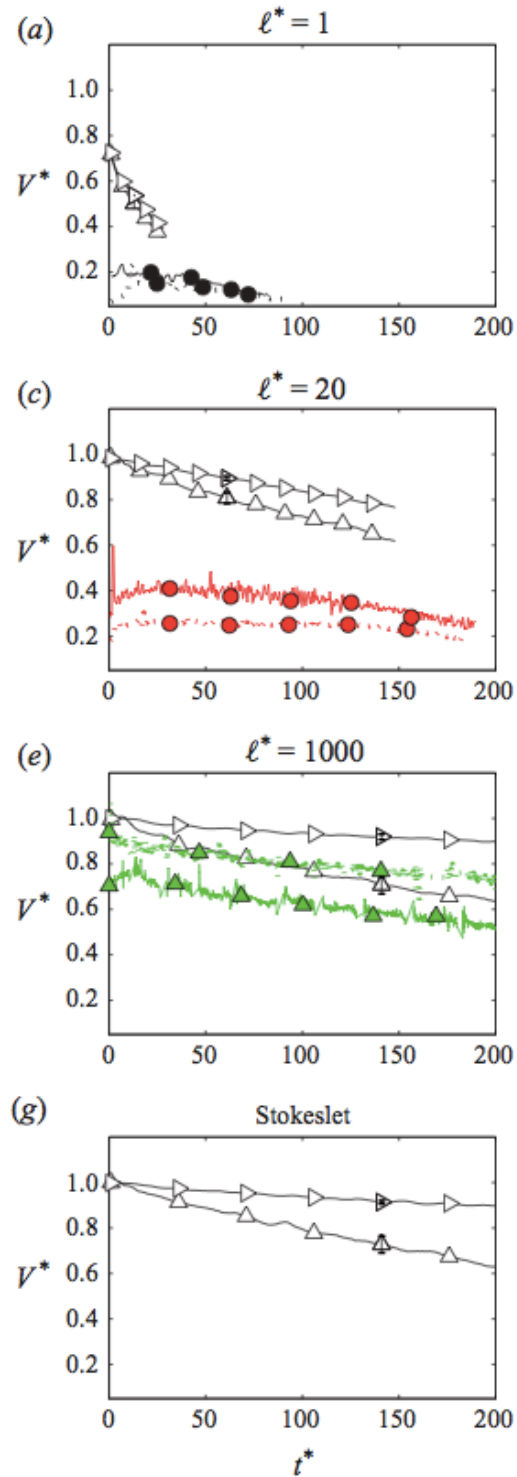


Figure 8: Droplet fall velocity versus time for simulations with Δ , $N = 500$; \triangleright , $N = 5000$, for different l^* values and Stokeslet conditions (From Pignatell et al., 2011).

As has been observed in many of the cases discussed, a falling suspension droplet will leak particles from the rear of the droplet to form a vertical tail. Comparing the streamlines of a droplet of pure liquid (see Figure 9) to those of a droplet of particles, Nitsche and Batchelor (1997) explain that the gravitational slip of the excess mass from the particles causes the boundary of the closed fluid streamlines, located on the edge of the droplet in the case of a pure liquid droplet, to shift to a location that is a finite distance inside of the droplet.

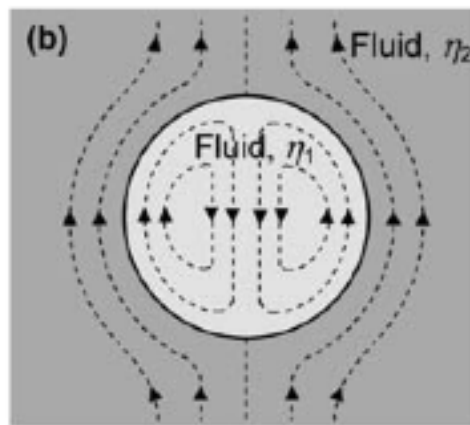


Figure 9: Streamlines of a droplet of pure liquid falling in an ambient fluid (From McHale et al.).

Nitsche and Batchelor illustrate the streamlines for a suspension droplet in Figure 10. The authors explain that the randomness of fluid velocities causes particles to cross over the boundary of the region of closed fluid streamlines, where they get swept out the rear of the droplet forming the vertical tail. Ekiel-Jezewska et al. (2006b) analytically derived this motion that occurs for suspension droplets, defining the radius of the inward shifted boundary of the closed streamlines (the closed Hadamard-Rybczynski toroidal circulation).

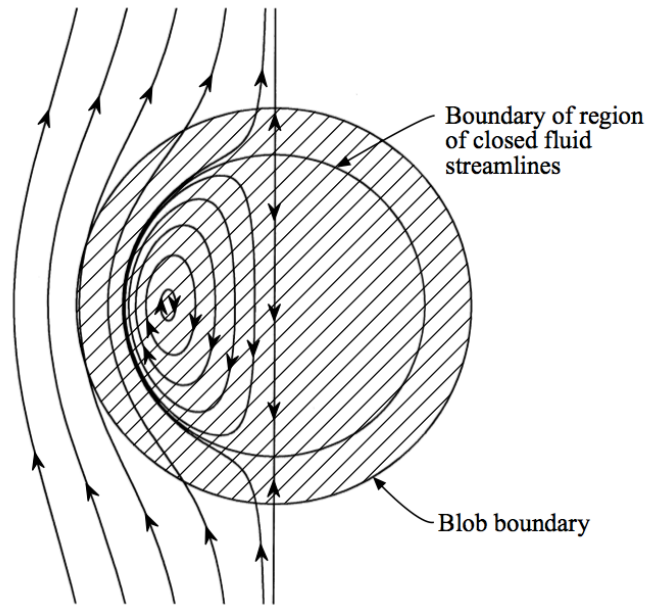


Figure 10: Streamlines of a suspension droplet falling in an ambient fluid, where the boundary of closed fluid streamlines is shifted a finite distance inside the boundary of the droplet due to the gravitational slip of the excess mass (From Nitsche & Batchelor, 1997).

Metzger et al. (2007) show computationally and experimentally that the percentage of particles that leak into the tail increases with decreasing initial number of particles in the droplet. This relationship is shown in Figure 11 from Metzger et al. (2007), which plots the percentage of particles in the tail versus time for different experimental runs with $N \approx 500$ (filled symbols) and $N \approx 2000$ (open symbols), and the average of several of the same numerical runs for $N \approx 500$ (dashed line) and $N \approx 2000$ (solid). Another important observation from this plot is that while there is significant variation between different runs of the same experimental case, the trends between the different runs are the same and are in agreement with the computations.

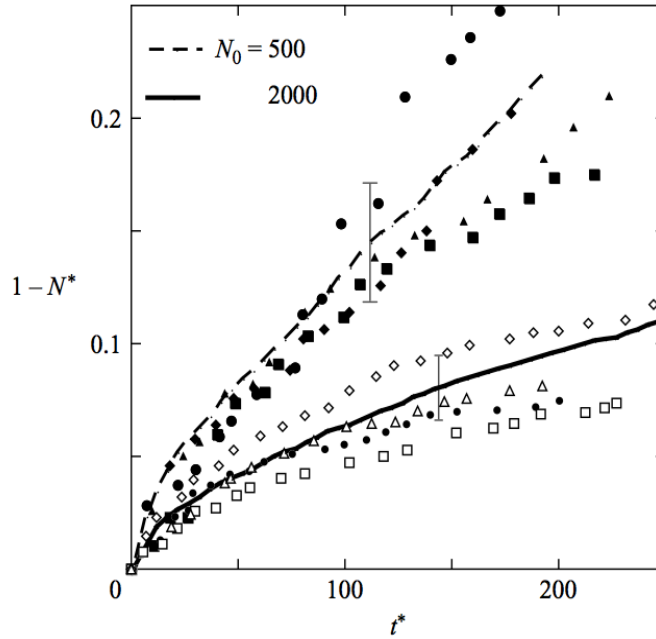


Figure 11: The percentage of particles that have leaked out of the droplet versus time. The dashed and solid lines represent averaged numerical runs for $N = 500$ and $N = 2000$ respectively. Different shapes represent different experimental runs under the same conditions, where filled shapes are for $N \approx 500$ and open shapes are for $N \approx 2000$ (From Metzger et al., 2007).

The authors compare these results to the inward shifted closed streamline boundary by evaluating the average departure D^* to the radius of the closed Hadamard-Rybczynski toroidal circulation boundary at each time step for runs with different numbers of particles. These results are plotted in Figure 12, and show that for blobs with lower number of particles, a higher percentage of particles cross over the recirculation region boundary.

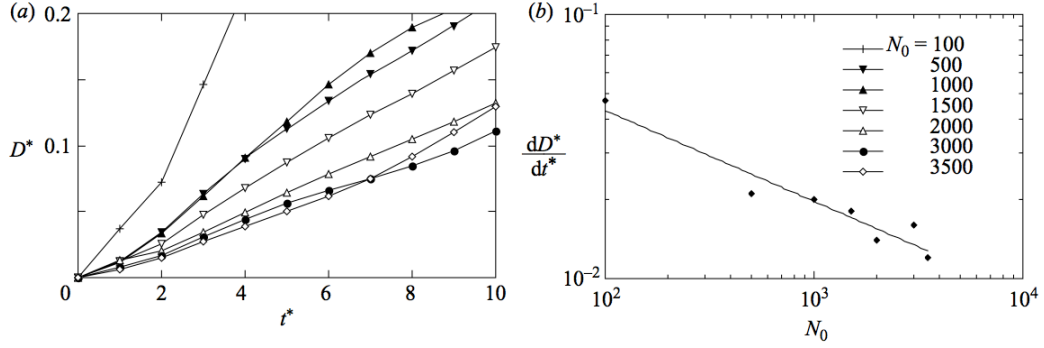


Figure 12: (a) The average departure distance from the Hadamard-Rybczynski toroidal closed streamlines (D^*) versus time for different values of N , and (b) the rate of departure dD^*/dt^* versus N (From Metzger et al., 2007).

Nitsche and Batchelor (1997) observe that the suspension droplet settles significantly more rapidly than would be predicted for a cloud of non-interacting particles due to the fluid motion induced by the particle settling. This observation led the authors (along with others, eg. Ekiel-Jezewska et al. (2006b)) to explore the use of (2.9) as a theoretical droplet fall velocity. Machu et al. (2001) formally proved the analogy between the behavior of suspension droplets and liquid droplets for the case where the particles in the suspension droplet are finely and uniformly dispersed throughout the blob when only the $O(1/r)$ far-field hydrodynamic interactions are important. The Stokesian dynamics simulations reported by Nitsche and Batchelor (1997) for small droplet Reynolds number yield fall velocities that were slightly higher than predicted by (2.9). Nitsche and Batchelor suggest that this difference is due to the fact that particles can slip relative to the surrounding fluid. Approximating the fluid slip velocity as equal to U , Nitsche and Batchelor propose a modified theoretical estimate for droplet fall velocity $U_{d,NB}$ as

$$\frac{U_{d,NB}}{U} = \frac{6}{5} N\epsilon + 1. \quad (2.10)$$

Pignatel et al. (2011) observe the droplet fall velocity to be substantially lower than predicted by the expression (2.9) for cases with finite droplet Reynolds number, and agreement for cases with small droplet Reynolds number. This is observed in Figure 13, which plots the experimental Re_d versus the initial number of particles in the droplet multiplied by the Re_p . The dashed line shows where $Re_d = 6NRe_p/5$, which corresponds to a Re_d computed from (2.9).

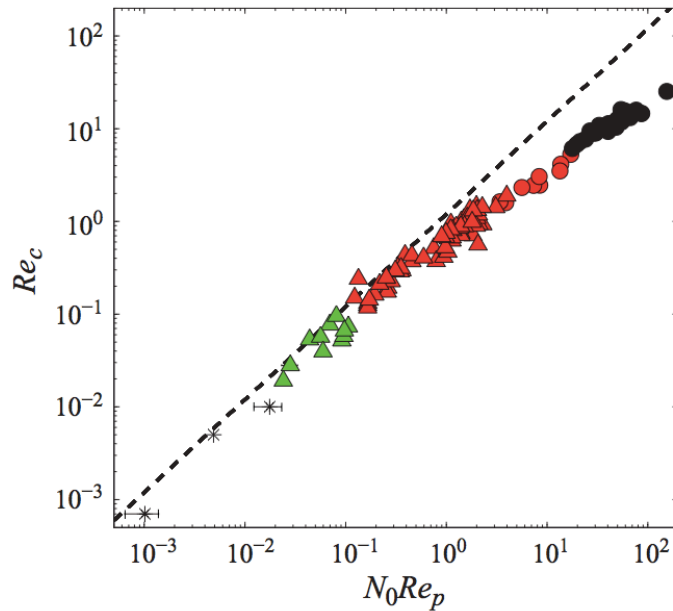


Figure 13: Experimental droplet Reynolds number (Re_c) versus the product of the initial number of particles in the droplet by the particle Reynolds number. The dashed line represents $Re_c = 6N_0 Re_p / 5$, and the symbols are the same as those in Figure 5 (From Pignatel et al., 2011).

Chapter 3

Computational Method

The numerical simulations were performed using a combination of the discrete-element method (DEM) for particle transport and collisions and a Lagrangian method for simulation of the fluid velocity fields at the particle locations. The fluid simulation method is similar to Stokesian dynamics, but it uses the full Oseen solution for the fluid velocity induced by each particle, which is necessary to account for finite droplet Reynolds numbers. By way of analogy, we call this extended computational method Oseen Dynamics.

3.1. Oseen Dynamics Simulation Method

One limitation of the Stokesian dynamics method is that it requires that the Reynolds number for the entire flow, i.e. the droplet Reynolds number Re_d , be small compared to unity throughout the flow. The reason for this restriction is that the Stokes solution is only valid within distances that are small compared to the inertial screening length $\ell = r_p / Re_p$ of the particle centroid. A uniformly valid solution for the flow

around a particle with low particle Reynolds number, $\text{Re}_p \ll 1$, is given by the Oseen solution (Proudman and Pearson, 1957). The Oseen solution for the flow field generated by a spherical particle with radius r_p translating with a velocity $U_s \mathbf{e}_x$ relative to the surrounding fluid at low particle Reynolds number Re_p can be written in a local spherical coordinate system, with the polar axis ($\theta = 0$) coincident with the direction of particle motion, as

$$u_r = \frac{U_s r_p^2}{r^2} \left\{ -\frac{r_p}{2r} \cos \theta - \frac{3(1 - \cos \theta)r}{4r_p} \exp \left[-\frac{\text{Re}_s r(1 + \cos \theta)}{2r_p} \right] + \frac{3}{2\text{Re}_p} \left(1 - \exp \left[-\frac{\text{Re}_s r(1 + \cos \theta)}{2r_p} \right] \right) \right.$$

$$u_\theta = -\frac{U_s r_p}{r} \sin \theta \left(\frac{r_p^2}{4r^2} + \frac{3}{4} \exp \left[-\frac{\text{Re}_s r(1 + \cos \theta)}{2r_p} \right] \right). \quad (3.1)$$

In this equation, $\text{Re}_s = 2r_p U_s / \nu$ is the instantaneous particle Reynolds number based on the particle slip velocity $U_s = |\mathbf{v} - \mathbf{u}|$, where \mathbf{v} is the particle velocity and \mathbf{u} is the fluid velocity at the particle centroid (evaluated as if the particle were not present). We note that Re_s varies with time on each particle as it moves about, whereas Re_p is a constant for a given suspension droplet flow, although both are the same order of magnitude. A schematic diagram illustrating the different regions of this flow field is shown in Figure 14. This solution approaches the Stokes solution for flow past a sphere within a region near to the particle, with distances $r \ll \ell$ away from the particle centroid. The velocity magnitude within this Stokes region decays with distance away from the particle as $O(1/r)$. At large distances from the particle, $r \gg \ell$, the velocity field within the far field

approaches a potential flow point source, whose velocity magnitude decays as $O(1/r^2)$.

The fluid emitted from this source is obtained from a back-flow within a thin wake region located near $\theta = \pi$, within which the velocity magnitude decays as $O(1/r)$.

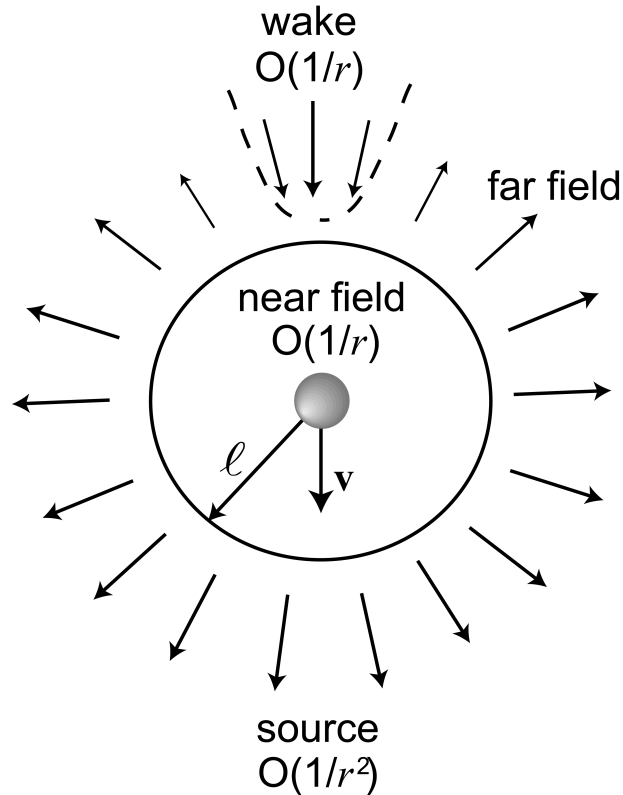


Figure 14: Schematic diagram illustrating the different regions in the velocity field induced around a spherical particle with radius r_p traveling with velocity v , according to the solution of the Oseen equations., drawn in a frame traveling with the particle. The velocity field reduces to the Stokes flow solution near the particle. In the far field, it has the form of a potential source, with $O(1/r^2)$ decay, and a thin wake region, with $O(1/r)$ decay. The transition region between the near and far fields occurs at a distance equal to the inertial screen length $\ell = r_p / \text{Re}_p$ away from the particle.

A comparison between the oseenlet solution for flow past a spherical particle and the sum of the stokeslet and potential doublet solution is shown for a case with particle

Reynolds number $Re_p = 0.1$ in Figure 15, which plots the velocity magnitude along rays emanating from the sphere centroid at different angles. For cases with $\theta = 0, \pi/4$ and $\pi/2$, the two solutions agree to within about 10% of each other for $r/r_p \leq 2$ and to within about 15% of each other for $r/r_p \leq 3$. The two solutions agree exactly for $\theta = \pi$, which corresponds with the wake region shown in Figure 14.

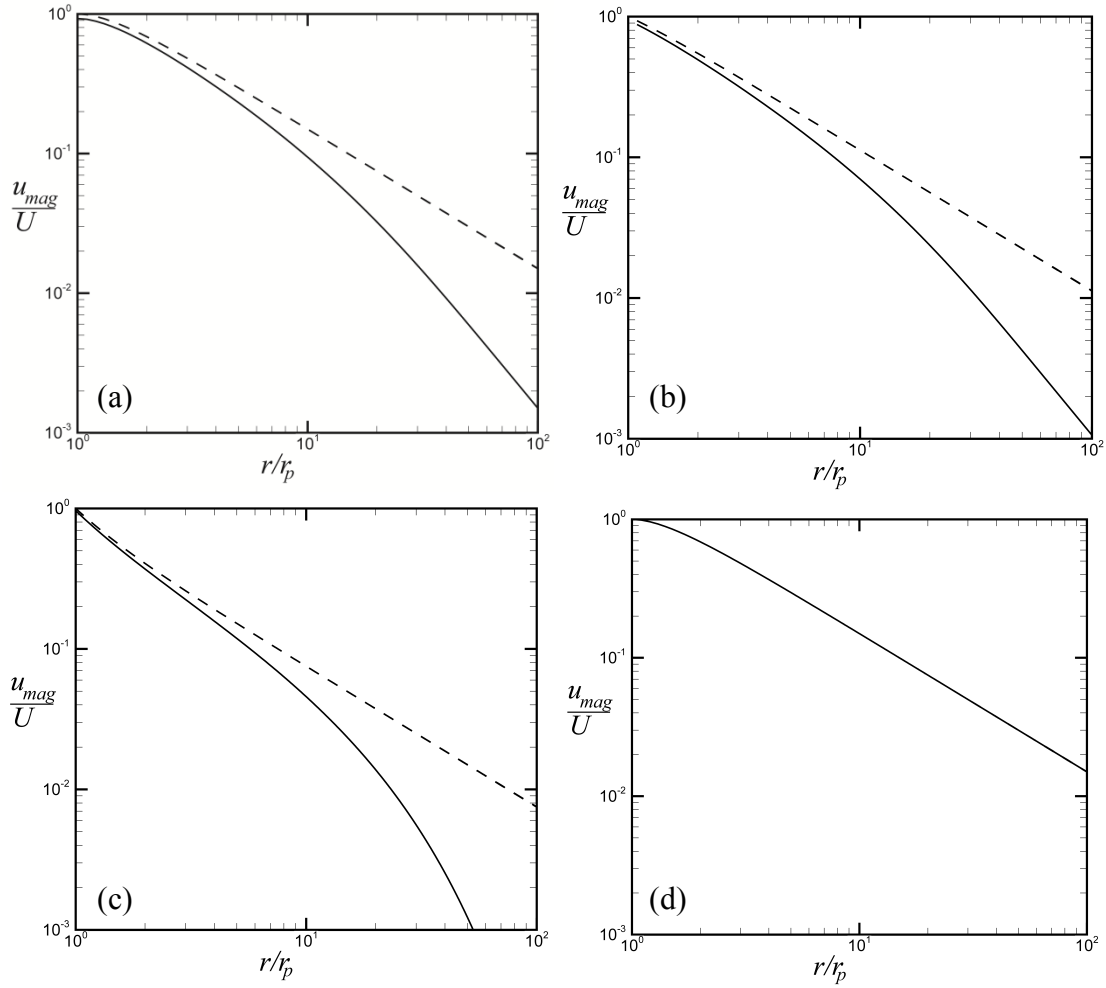


Figure 15: Comparison of the dimensionless velocity magnitude as a function of distance for a Stokeslet plus a potential doublet (dashed line) and for the Oseenlet solution (solid line) along a ray starting from the sphere centroid, with angles (a) $\theta = 0$, (b) $\pi/4$, (c) $\pi/2$, and (d) π . The computations are for a case with particle Reynolds number $Re_p = 0.1$.

The fluid velocity \mathbf{u}_i at the centroid of particle i , where $i = 1, \dots, N$, is obtained at each time step by solution of a matrix equation of the form

$$\mathbf{u}_i = \sum_{j \neq i} \mathbf{W}(\mathbf{x}_i, \mathbf{x}_j)(\mathbf{v}_j - \mathbf{u}_j). \quad (3.2)$$

The matrix \mathbf{W} is obtained using (3.1) after rotating the local spherical coordinate system into a global coordinate frame. Unlike the Stokesian dynamics problem, the matrix \mathbf{W} depends on the fluid velocity through the Reynolds number. Equation (3.2) is solved for \mathbf{u}_i using a Gauss-Seidel iteration method with quasi-linearization, in which the dependence of \mathbf{W} on Re_s is lagged one iteration. The iterations are continued to a prescribed relative error of 10^{-5} . This iterative approach is both much faster than the direct solution of the matrix problem and it avoids having to form the matrix \mathbf{W} .

3.2. Particle Motion

The discrete-element method (DEM) is used to transport non-adhesive particles in the flow field. The computational method uses a multiple time step algorithm, in which the fluid time step $\Delta t = O(L/U)$, the particle time step $\Delta t_p = O(d/U)$, and the collision time step $\Delta t_c = O(d(\rho_p^2/E_p^2U)^{1/5})$ satisfy $\Delta t > \Delta t_p > \Delta t_c$. Here d is the particle diameter, ρ_p is the particle density, and E_p is the particle elastic modulus. The characteristic fluid length and velocity scales, L and U , are set equal to the suspension

droplet initial diameter ($L = 2r_d$) and the terminal settling velocity of an isolated particle, respectively. The method follows the motion of individual particles in the three-dimensional fluid flow by solution of the particle momentum and angular momentum equations

$$m \frac{d\mathbf{v}}{dt} = \mathbf{F}_F + \mathbf{F}_A + \mathbf{F}_G, \quad I \frac{d\mathbf{\Omega}}{dt} = \mathbf{M}_F + \mathbf{M}_A, \quad (3.3)$$

subject to forces and torques induced by the fluid flow (\mathbf{F}_F and \mathbf{M}_F), by particle collision (\mathbf{F}_A and \mathbf{M}_A), and by gravity (\mathbf{F}_G). Here, m is the particle mass, I is the moment of inertia, and \mathbf{v} and $\mathbf{\Omega}$ are the particle velocity and rotation rate, respectively.

The reduced gravity force \mathbf{F}_G on the particle is given by

$$\mathbf{F}_G = -\frac{\pi}{6} d^3 (\rho_p - \rho_f) g \mathbf{e}_y, \quad (3.4)$$

where gravity is assumed to act in the negative y -direction. This force includes both the gravitational force and the buoyancy force of the particle under the hydrostatic pressure gradient. The drag force is given by the Stokes drag law as

$$\mathbf{F}_d = 3\pi\mu d(\mathbf{u} - \mathbf{v}). \quad (3.5)$$

The added mass force \mathbf{F}_a is given by

$$\mathbf{F}_a = -c_M \frac{\pi}{6} \rho_f d^3 \left(\frac{d\mathbf{v}}{dt} - \frac{d\mathbf{u}}{dt} \right). \quad (3.6)$$

The total force on the particle is taken as the sum of these three forces. The viscous fluid torque on the particle is given by

$$\mathbf{M}_F = -\pi\mu d^3 \left(\boldsymbol{\Omega} - \frac{1}{2} \boldsymbol{\omega} \right), \quad (3.7)$$

where $\boldsymbol{\omega}$ is the fluid vorticity at the particle centroid.

Particle collisions are simulated by employing a soft-sphere collision model, where each collision includes a normal force F_n along the line with unit vector $\mathbf{n} = (\mathbf{x}_j - \mathbf{x}_i) / |\mathbf{x}_j - \mathbf{x}_i|$ connecting the centroids of two particles, with positions \mathbf{x}_i and \mathbf{x}_j , as well as frictional resistances for sliding and twisting motions. For a particle of radius r_i , we can write

$$\mathbf{F}_A = -F_n \mathbf{n} + F_s \mathbf{t}_S, \quad \mathbf{M}_A = r_p F_s (\mathbf{n} \times \mathbf{t}_S) + M_t \mathbf{n}. \quad (3.8)$$

A positive value of the normal force F_n corresponds to a repulsive force between the particles. The unit vector $\mathbf{t}_S \equiv \mathbf{v}_S / |\mathbf{v}_S|$ indicates the direction of sliding between the two particles, where the slip velocity \mathbf{v}_S is defined by $\mathbf{v}_S = \mathbf{v}_R - (\mathbf{v}_R \cdot \mathbf{n})\mathbf{n} + r_p \boldsymbol{\Omega}_i \times \mathbf{n} + r_p \boldsymbol{\Omega}_j \times \mathbf{n}$ and $\mathbf{v}_R = \mathbf{v}_i - \mathbf{v}_j$ is the particle relative velocity. The normal force F_n is composed of the sum of the elastic force F_{ne} and a dissipative force F_{nd} . The normal force is given in terms of the normal overlap $\delta_N = 2r_p - |\mathbf{x}_i - \mathbf{x}_j|$ by the Hertz expression (Hertz, 1882) as

$$F_{ne} = K\delta_N^{3/2}, \quad (3.9)$$

where K is written in terms of the effective elastic modulus $E \equiv [(1 - \sigma_i^2)/E_i + (1 - \sigma_j^2)/E_j]^{-1}$ as $K = (4/3)E\sqrt{r_p/2}$. Here σ_i and E_i are the Poisson ratio and elastic modulus of particle i , respectively.

There are numerous expressions in the literature for the dissipative normal force F_{nd} , but in the current paper we utilize the simple form proposed by Tsuji et al. (1992) in which F_{nd} depends linearly on the normal component of \mathbf{v}_R . The Stokes number in the current paper is sufficiently small that the particle restitution coefficient can be taken to be zero. Sliding resistance is based on a spring-dashpot-slider model similar to that proposed by Cundall and Strack (1979) with friction coefficient $\mu_f \cong 0.3$. The twisting resistance is dependent on the relative twisting rate $\Omega_T \equiv (\boldsymbol{\Omega}_i - \boldsymbol{\Omega}_j) \cdot \mathbf{n}$ between two particles. We use a rotational spring-dashpot-slider model for twisting resistance developed by Marshall (2009), in which the twisting torque is absorbed by the rotational spring and dashpot until the torque reaches a critical magnitude $M_{t,crit}$.

Chapter 4

Computational Results

The governing equations for the suspension droplet motion can be non-dimensionalized by selecting the characteristic fluid length and velocity scales as the initial droplet diameter $L = 2r_d$ and the terminal settling speed U of an isolated particle of nominal size and density, where the latter is given by

$$U = \frac{d^2 g_R}{18\nu\chi}, \quad (4.1)$$

and $g_R = (1 - \chi)g$ is the reduced gravitational acceleration. Since we consider computations with variable size and density particles, it is convenient to define a nominal particle density $\bar{\rho}_p$ and diameter \bar{d} by

$$\bar{\rho}_p = \frac{1}{N} \sum_{n=1}^N \rho_n, \quad \bar{d} = \left(\frac{1}{N} \sum_{n=1}^N d_n^2 \right)^{1/2}, \quad (4.2)$$

where N is the number of particles. The nominal particle diameter is specified by averaging the square of the diameter to ensure that the average terminal velocity (for an isolated particle) will be equal to that for particles whose diameter are equal to the nominal value \bar{d} . In (4.1), $\chi = \rho_f / \bar{\rho}_p$ is the ratio of the fluid density to the nominal

particle density. The Froude number $Fr = U / \sqrt{g_R L}$ and the Stokes number $St = \bar{\rho}_p \bar{d}^2 U / 18 \mu L$ for this flow can be expressed in terms of the particle Reynolds number as

$$St = Fr^2 = \frac{Re_p}{18\chi} (\bar{d}/L)^2. \quad (4.3)$$

The results plotted in the paper are in terms of dimensionless variables in which all length scales are nondimensionalized by L , all velocity scales are nondimensionalized by U computed using (4.1) with the nominal particle diameter and density, and all time scales are nondimensionalized using L/U . Dimensionless variables are denoted by an asterisk. In all of the computations, the initial conditions consist of an initially spherical suspension droplet placed in a static liquid.

4.1. Suspension Droplets with Uniform Particle

Properties

For uniform size and density particles, the independent dimensionless parameters of the flow include Re_d , $\varepsilon \equiv \bar{d}/L$, χ , and the number of particles N_0 initially contained within the droplet. Several studies for uniform-size particles have been reported in the literature (Nitsche and Batchelor, 1997; Metzger et al., 2007; Subramanian and Koch, 2008; Pignatell et al., 2011), which detail how the droplet fall velocity and shape change with variation of these parameters. An important characteristic of the falling suspension droplet noted in this literature is the tendency of the falling

droplet to develop a tail, formed of particles that leak away from the droplet near the droplet rear. In the current work, we repeat some of these calculations for uniform particles in order to establish a baseline with which to compare results for non-uniform particle density and size. Since the primary purpose of the paper is to examine effects of particle size and density variation, we will confine the computations to a limited range of parameters. In particular, the computations focus on variation in droplet Reynolds number, so that the other parameters are fixed to have values $\bar{d}/L = 0.04$, $\chi = 1/3$, and $N_0 = 300$.

A plot showing a time series of particle positions for a typical case with $Re_d = 144$ is given in Figure 16. This plot illustrates the suspension droplet falling as a ball, but with a tail of trailing particles shed from the rear of the droplet gradually developing. The tail grows progressively longer with time since the particles within the tail fall at nearly the terminal velocity for an isolated particle, whereas the particles within the droplet fall at a much faster rate due to the hydrodynamic interaction between the particles. The droplet shape also becomes deformed in time, with a slight flattening of the ball-like shape in the vertical direction.

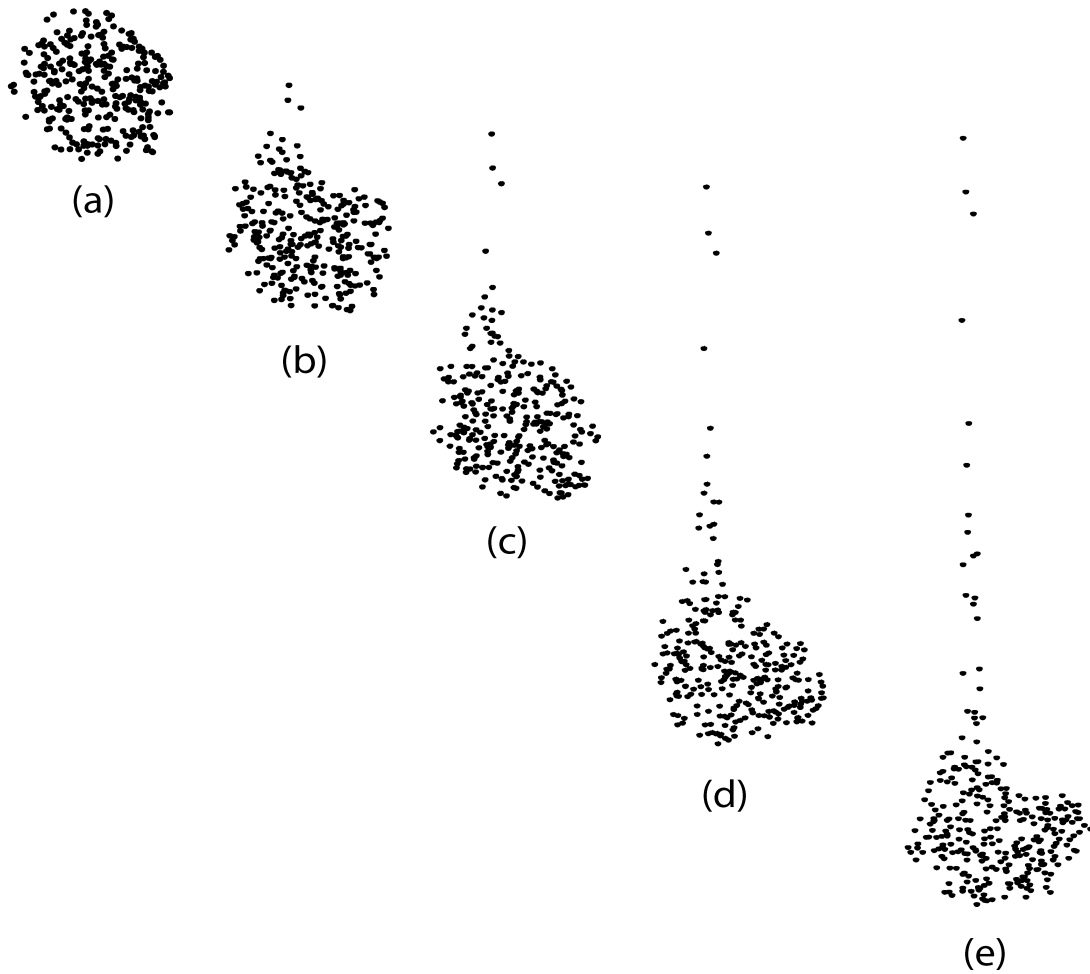


Figure 16: Plot showing formation of tail behind a falling suspension droplet for a computation with a uniform particle type and $Re_d = 10$. Images are shown at times (a) $t^* = 0$, (b) 0.6, (c) 0.8, (d) 1.0 and (e) 1.2.

A contour plot of the fluid velocity magnitude, with fluid streamlines and particles superimposed, is plotted in Figure 17 at time $t^* = 4.5$ for the case of $Re_d = 144$, in a frame moving with the droplet. The fluid velocity field has a toroidal form, which is qualitatively similar to the Hill's spherical vortex. Stagnation points in this convected

frame occur both at the front and rear of the droplet, as well as within the core of the vortex ring structure.

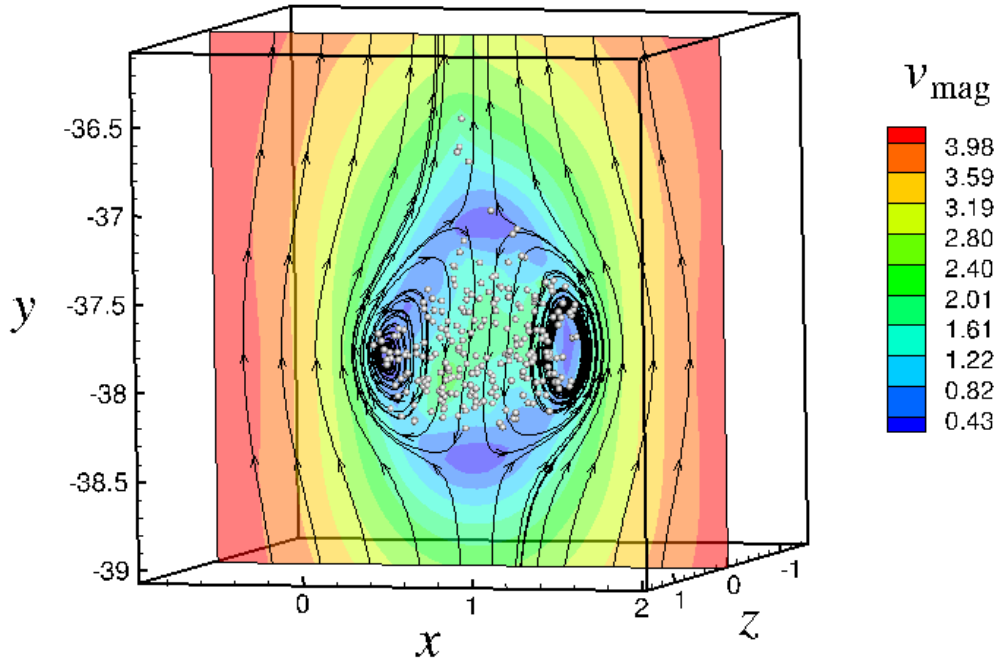


Figure 17: Contour plot of fluid velocity magnitude within a falling suspension droplet, with superimposed fluid streamlines and particles, at time $t^* = 4.5$ for the case of uniform particles.

The average y -position of the particles is plotted as a function of time in Figure 18a for cases with $\text{Re}_d = 58, 144$ and 360 , and the corresponding fall velocity $v_{\text{ave}}^* = -dy_{\text{ave}}^* / dt^*$ is plotted in Figure 17b. It is noted that v_{ave}^* is the average velocity of all the particles, not just the particles in the droplet. The fall velocity reaches a maximum value at about $t^* = 0.7$, which is also the time at which the particle tail starts to shed from the droplet. In all cases examined, the peak magnitude of the fall velocity is substantially greater than unity, indicating that the suspension droplet falls much faster

than an isolated particle. The droplet fall velocity decreases for dimensionless times t^* greater than 0.7 as the particles gradually move from the droplet into the tail and the tail grows progressively longer.

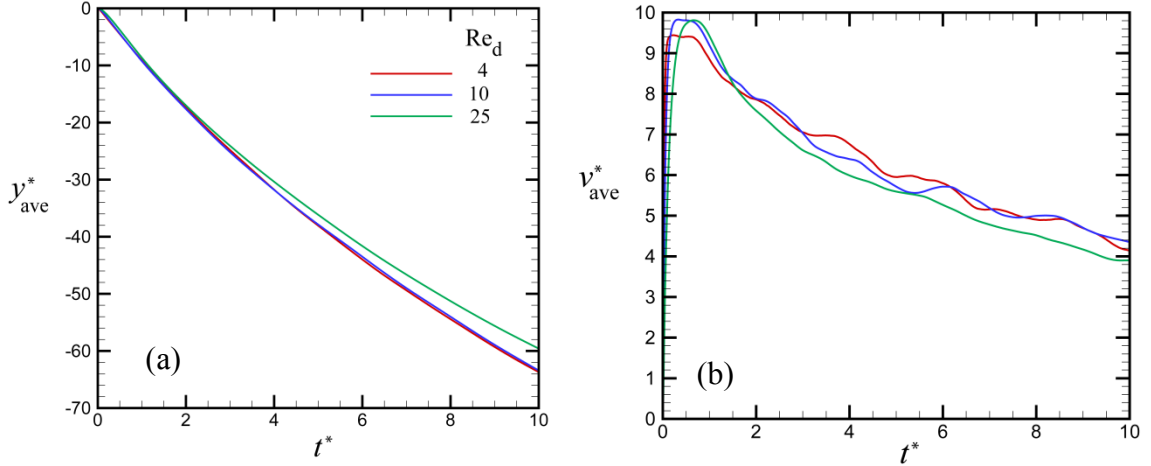


Figure 18: Plot showing the time variation of the (a) average y -position and (b) fall velocity for a droplet of uniform size particles at different droplet Reynolds numbers.

The percentage P of the initial particles that remain in the droplet at dimensionless time t^* is plotted in Figure 19a. In order to allow some deformation of the suspension droplet, we compute P using an effective droplet diameter equal to $1.25L$, which is 25% larger than the nominal droplet diameter. In Figure 19a, all particles are observed to fall within the droplet for a short time at the beginning of the computation (approximately $t^* < 0.7$), but then formation of the droplet tail leads to a gradual decrease in number of particles within the droplet. Using the data for the current number of particles $N(t)$ contained within the droplet at time t , we compute the ratio $U_d^*(t)/[\frac{6}{5}N(t)\varepsilon]$ of the computed droplet settling velocity U_d^* and the theoretical droplet fall velocity based on the current number of particles within the droplet. Oscillations in

some of the data are due to shape oscillations of the droplet. The computed fall velocities agree within about 30% with the solution (2.9), although similar to Pignatel et al. (2011) we observe the fall velocities at finite droplet Reynolds number to be somewhat below the theoretical solution. While both U_d^* and N decrease substantially in time after the peak velocity is reached, the ratio in Figure 19b is nearly constant in time. This fact confirms that the computational predictions satisfy the linear scaling between U_d^* and N predicted by the theoretical expression (2.9).

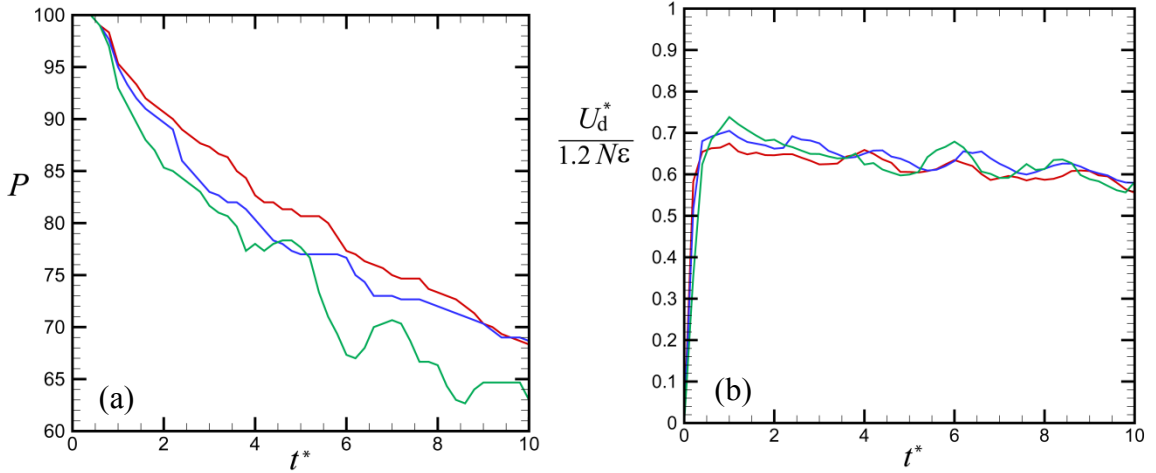


Figure 19: Time variation of (a) the percentage of particles that remain in the droplet and (b) the computed average fall velocity divided by the solution (2.9). The plots are for uniform droplet size and different droplet Reynolds numbers, and the color legend is the same as used in Figure 18.

Two measures of the length of the particle tail are shown in Figure 20– the root-mean-square position y_{rms}^* of the particles in the y -direction and the ratio $(y_{max}^* - y_{min}^*)/4$ of the maximum and minimum particle positions divided by 4. For particles that are uniformly distributed between y_{max}^* and y_{min}^* , this measure is equal to the root-mean-square position y_{rms}^* , so the difference between these two measures provides an

indication of the skewness of the particle positions within this interval. The value of y_{rms}^* remains close to the value for a uniform sphere for $t^* < 1$, after which the growth of the droplet tail causes y_{rms}^* to increase nearly linearly with time. The value of $(y_{max}^* - y_{min}^*)/4$ is larger than the corresponding value of y_{rms}^* , as is consistent with the fact that the presence of the droplet implies a large number of particles with values of y^* near y_{min}^* . Over time, the two measures appear to approach each other as an increasing number of the particles are drawn out into the tail region.

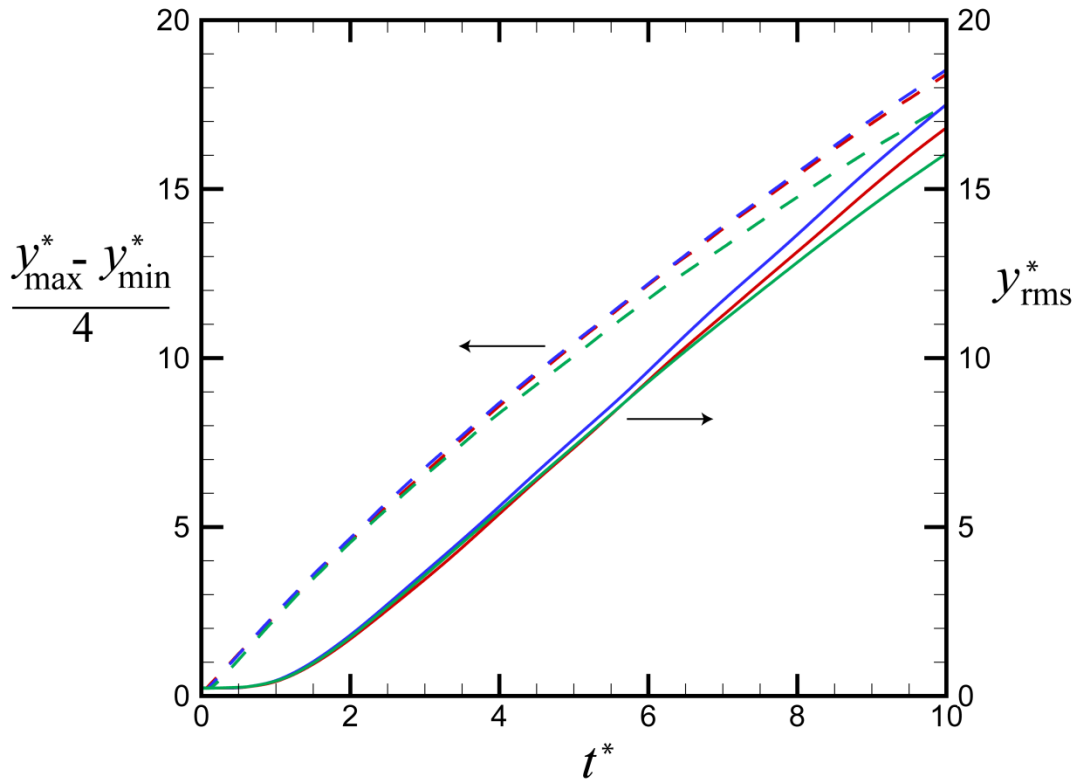


Figure 20: Plot showing the time variation of the root-mean-square y -position and the value of $(y_{max}^* - y_{min}^*)/4$ for a droplet of uniform size particles at different droplet Reynolds numbers. The color legend is the same as used in Figure 18.

The various results in Figure 18- Figure 20 exhibit little influence of Reynolds number. This does not mean that the actual fall velocity and other parameters are independent of fluid viscosity, but instead that the effect of fluid viscosity on these parameters varies in the same proportion as the viscosity effect on the fall velocity U of an isolated particle, which is used to nondimensionalize the velocity and time variables used in these plots. In addition to being consistent with the expression (2.9) for droplet fall velocity U_d^* , this scaling is consistent with the theoretical observation from Nitsche and Batchelor (1997) that the rate of particles lost to the droplet is proportional to the settling velocity for a single particle, U . If we assume that $dN/dt = CU$, where C is independent of fluid viscosity, then defining a dimensionless time by $t^* = tU/L$ results in the observation that dN/dt^* should be independent of Reynolds number. As a consequence, one would expect that the percentage of particles P remaining within the droplet and the dispersion measures y_{rms}^* and $(y_{max}^* - y_{min}^*)/4$ will be independent of Reynolds number, which is reasonably consistent with the results in Figure 19a and Figure 20.

4.2. Suspension Droplets with Variable Particle Density

In this section, we examine suspension droplets with particles of uniform size, but with some particles having a larger density than the other particles. For such problems, we add to the set of dimensionless parameters the relative difference in particle density

$\beta \equiv |\rho_{p2} - \rho_{p1}| / 2\bar{\rho}_p$ and the particle number ratio N_1 / N_2 . For all simulations reported in this section there are equal number of heavy and light particles, so $N_1 / N_2 = 1$.

We begin by examining the effect of droplet concentration on the segregation phenomena of particles with different densities by comparing results of suspension droplet computations with total initial number of particles $N_0 = 50$ and $N_0 = 300$, where all other parameters are held constant at $\beta = 0.5$, $\bar{d} / L = 0.04$, $\chi = 1/3$, and $\text{Re}_d = 10$. Plots showing the time series of particle positions for $N_0 = 50$ and $N_0 = 300$ are given in Figure 21 and Figure 22, respectively. In the case with lower particle concentration (Figure 21), the weak hydrodynamic interaction between the particles is insufficient to stop the separation of light and heavy particles that occurs due to their different fall velocities. Consequently, the light particles quickly separate from the suspension droplet as a dispersed cloud. The particle hydrodynamic interaction is sufficiently strong that this cloud of light particles becomes stretched in the direction of gravity during the separation process, but nevertheless, the separation occurs relatively quickly (after the suspension droplet has fallen a distance equal to a few droplet diameters) and the particles of both types remain grouped in a cloud-like shape.

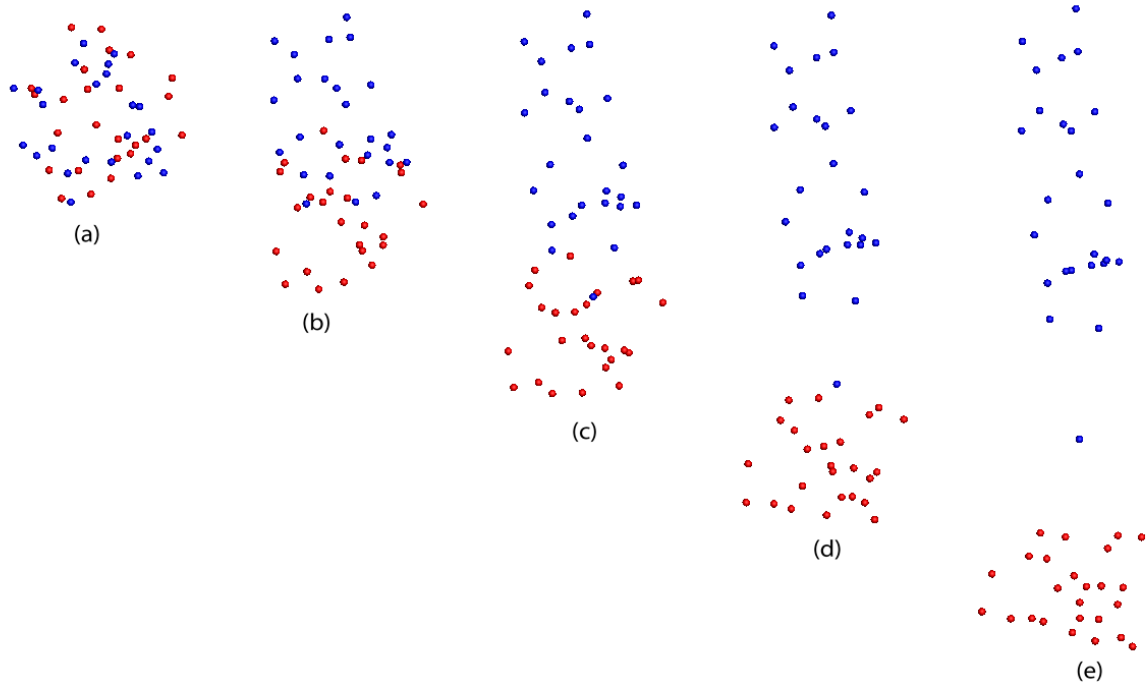


Figure 21: Time series of a droplet with $N = 50$, for a case with particles of two densities where $\beta = 0.5$. Images are shown at times (a) $t^* = 0$, (b) 0.6, (c) 1.0, (d) 1.4 and (e) 1.8. The light particles are shown in blue and the heavy particles in red.

The case with higher particle concentration shown in Figure 22 has much greater hydrodynamic interaction forces between the particles, and consequently the suspension droplet dynamics are quite different than observed in Figure 21. Most noticeably, it is observed that some of the light particles are able to remain inside the suspension droplets for long periods of time for cases with sufficiently high values of the particle concentration. Similar to the simulations for particles of uniform density, the suspension droplet falls with nearly a spherical shape with a tail of trailing particles shed from the rear of the droplet. As time passes, the tail grows progressively longer because the particles in the tail are falling at approximately the terminal velocity of an isolated particle, whereas the particles in the droplet fall much faster due to the hydrodynamic

interaction between the particles in the droplet. A striking feature of Figure 22 is the fact that nearly all of the particles within the tail region are the lighter particles, whereas the heavier particles largely remain within the droplet. Over longer time intervals than shown in this figure, we observe that the heavier particles do eventually start to enter into the tail, but at a lower rate than the lighter particles. Eventually all of the light particles are removed from the droplet and form a very long tail behind the suspension droplet, after which the rate at which particles enter into the tail decreases significantly.

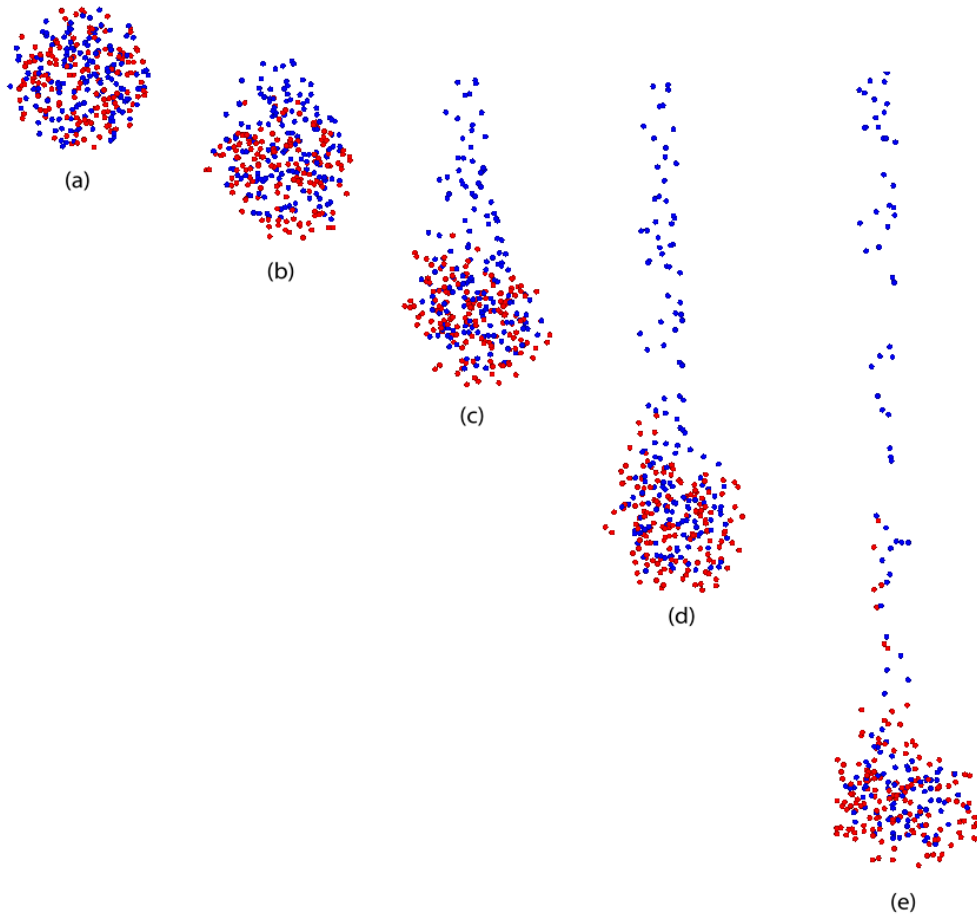


Figure 22: Time series of a droplet with $N = 300$, showing preferential leakage of lighter particles into the droplet tail, for a case with particles with two densities with $\beta = 0.5$.

Images are shown at times (a) $t^* = 0$, (b) 0.2, (c) 0.4, (d) 0.6 and (e) 1.0. The light particles are shown in blue and the heavy particles in red.

This latter case, in which the suspension droplet dynamics is dominated by hydrodynamic interaction between the particles, is of particular interest to us. To explore this case further, we report results of a series of computations with different values of β , but with all other parameters fixed to the same values as used for the simulation shown in Figure 22. The average particle fall velocity $v_{ave}^* = -dy_{ave}^* / dt^*$ is plotted as a function of time in Figure 23a for values of β ranging between 0 and 0.75. This velocity is computed separately for the light and heavy particles, which are plotted in Figure 23a using dashed and solid curves, respectively. The fall velocity of all particles reaches a maximum value at about $t^* = 0.7$, with approximately the same value for both light and heavy particles. The value of v_{ave}^* decreases with time after this peak value is achieved, which is associated with the decrease in number of particles in the droplet as a result of tail formation. Because the light particles move rapidly into the tail, the average fall velocity of the light particles decreases with time much more quickly than it does for the heavy particles. Since the isolated particle velocity (and hence also the fall velocity of particles in the tail) decreases with decrease in particle density ρ_n , the rate at which the fall velocity of the light particles decreases in time in Figure 23a increases with increase in β (and hence reduction in density of the light particles). Since most of the heavy particles remain in the droplet, the average fall velocity of the heavy particles is nearly independent of β , and it is approximately the same as the fall velocity for uniform size particles.

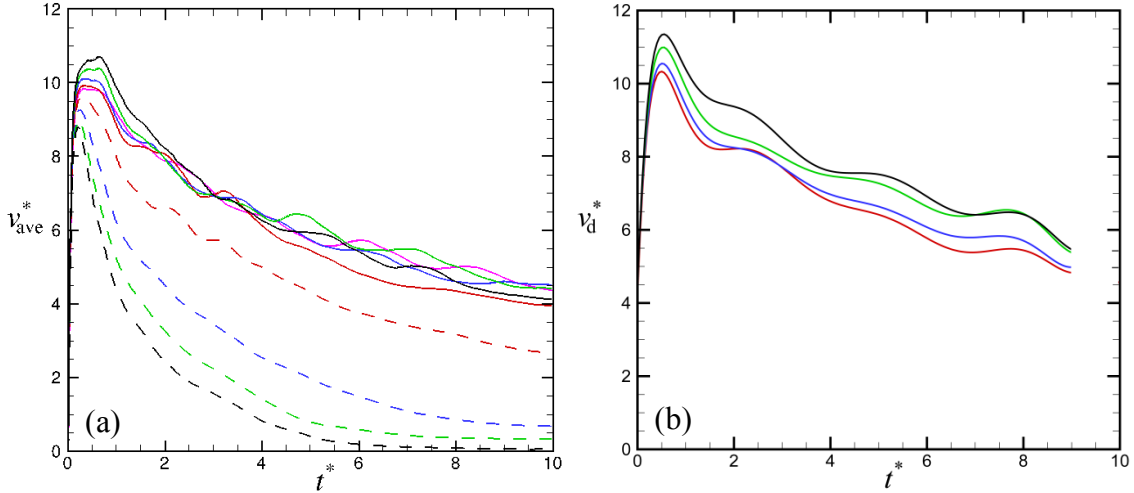


Figure 23: (a) Comparison of the average fall velocity of the heavy particles (dark lines) and the light particles (dashed lines) plotted with time for varying β . (b) Comparison of the droplet fall velocity for varying β plotted with time. $\beta = 0$ (pink line), 0.25 (red lines), 0.5 (blue lines), 0.65 (green lines), and 0.75 (black lines).

The droplet fall velocity is plotted with time for different values of β in Figure 23b. The data is smoothed by plotting the droplet fall velocity with a 9th order polynomial. The slight oscillations observed in the plot are due to slight droplet shape changes that affect the calculated values due to the way in which the droplet fall velocity was calculated. There is not much variation in the droplet velocity value between cases with different β values, but the droplet velocity does slightly increase with increasing β value. Comparing Figure 23a and Figure 23b, the droplet fall velocity values are similar to the average velocity values of the heavier particles.

The degree of particle spread in the vertical direction within the tail and droplet is quantified using the root-mean-square position of the particles in the y -direction, y_{rms}^* . This quantity is plotted as a function of time in Figure 24 for each particle type, along with the percentage P of particles of a given type remaining in the droplet. It is noted that

small values of y_{rms}^* can be achieved either if particles all remain in the droplet or if particles are quickly removed from the droplet into the tail. The largest values of y_{rms}^* occur when particles move very slowly from the droplet into the tail. For the heavier particles (indicated by solid lines in Figure 24), the particles with densities closest to the nominal density (small β) have the smallest values of y_{rms}^* and the largest values of P , and particles with higher densities (larger β) have larger values of y_{rms}^* and smaller values of P . A similar trend holds for the lighter particles (dashed lines in Figure 24), although the differences are much greater for different β values. The reason for this trend is that the rapid separation of light particles from the droplet for cases with large β causes a significant relative velocity between particles of different densities, which leads to more frequent collisions that bump a larger number of the heavier particles out of the droplet compared to cases with smaller β . The mechanisms for removal of both light and heavy particles from the droplet are discussed in detail in Section 4.

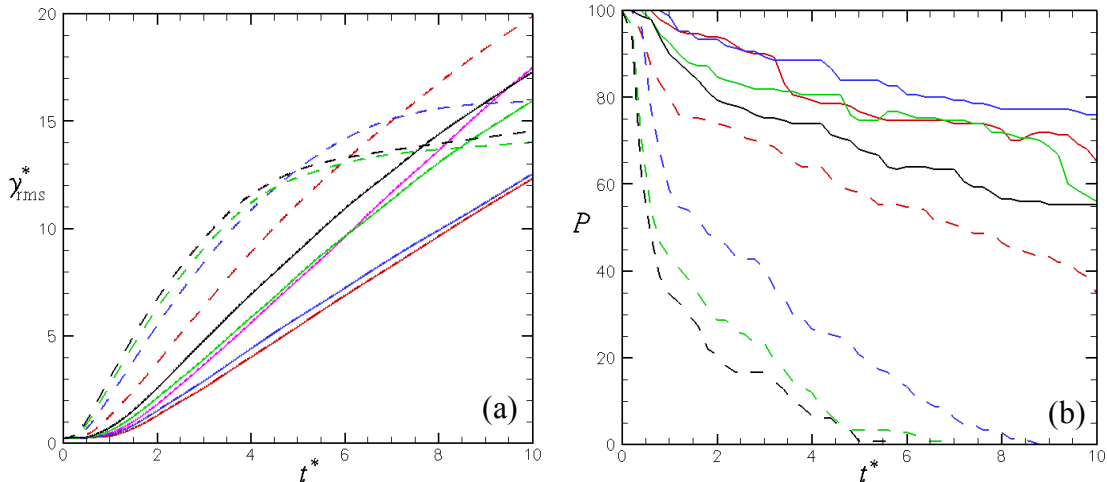


Figure 24: Plot of (a) y_{rms}^* and (b) percentage of particles P remaining in the droplet as a functions of time with different values of β , comparing values for the heavy particles

(solid lines) and for the light particles (dashed lines). The plot uses the same legend as in Figure 23.

While y_{rms}^* increases almost linearly in time for the heavier particles, for the lighter particles y_{rms}^* initially increases in a linear fashion but then asymptotes to a nearly constant value at long time. The time at which this flattening behavior is reached decreases as the value of β increases. This flattening behavior corresponds to a state in which all of the lighter particles have been removed from the droplet, and is indicated in Figure 24b by a state where $P = 0$. Since all of the light particles in the tail fall at approximately the same speed, the value of y_{rms}^* for the light particles remains approximately constant once the light particles are removed from the droplet. The case with $\beta = 0.25$ has a much smaller density difference than the other cases, and this case has not yet reached a point where all of the light particles are removed from the droplet by the end of the computation.

There are numerous mixing and segregation indices used in the literature, many of which are adopted for specific problems. For instance, in experiments involving mixing of particles of two different sizes or densities in a two-dimensional rotating drum, Jain et al. (2005) define a segregation index based on the geometric mean of the area covered by only one particle type and that occupied by a mixed blend of particles of two sizes, normalized by the total area covered by particles. This approach, and others like it, cannot be used when there is a variation in particle concentration, as is the case in a suspension, and can only be used when there are clearly distinguished regions occupied

by a single type of particle. Li and McCarthy (2005) proposed a segregation measure, again for rotating drum mixing flows, based on the root-mean-square of the concentration field of a particle of a given type. This measure is useful for fully packed granular systems where the only differences in concentration are due to segregation, but it is not as useful for particle suspensions, in which there may be significant variation in concentration field due to flow processes or due to the method used to compute the concentration (Marshall and Sala, 2013), even in systems with uniform particle size and density. Shinohara and Golman (2002) propose a set of segregation measures for hopper flows with a broad particle distribution, but these measures are not very useful for bimodal mixtures.

A mixing index proposed for DEM simulations by Amar et al. (2002) would seem to be applicable for the problem addressed in the current paper. In this paper, a generalized mean mixing index is defined for a given coordinate direction (say, y) as

$$G_i = \left[\frac{1}{N_i} \sum_{j=1}^{N_i} (y_j - y_{ref}) \right] / \left[\frac{1}{N_{tot}} \sum_{k=1}^{N_{tot}} (y_k - y_{ref}) \right]. \quad (4.4)$$

In this equation, the numerator is a sum over all N_i particles of type i , whereas the denominator is a sum over all N_{tot} particles in the system. A value of G equal to 1 indicates that particle type i is distributed within the solution domain in a similar manner to all of the other particles. A value of G less than 1 indicates that particles of type i tend to have lower value of y than the average value for the entire particle set, and a value greater than 1 indicates that particle of type i tend to have higher values of y than the average value for the entire particle set.

The mixing measure G_{light} for the light particles is plotted as a function of time for different values of β in Figure 25. The initial value of G_{light} is equal to unity for all cases, indicating that the initial condition is well mixed. For small values of t^* , the value of G_{light} increases with time as the lighter particles preferentially segregate into the droplet tail. At some point around $t^* \approx 2$ or so, a maximum value of G_{light} is attained, after which the mixing measure gradually decreases for the remainder of the computation as the larger particles begin to enter into the droplet tail in larger numbers. The value of the mixing measure is found to exhibit a marked increase with increase in β , indicating that the extent of particle segregation becomes substantially greater as the density difference between the particles increases. The trend breaks down for $\beta > 0.5$, where we notice that the three cases with $\beta = 0.5, 0.65$ and 0.75 all have similar values of the mixing measure.

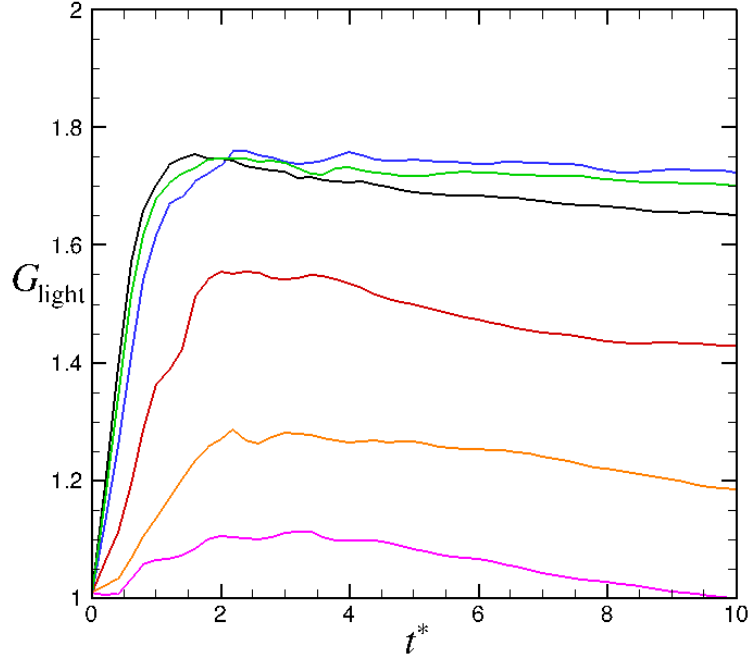


Figure 25: Plot showing time variation of the mixing index G_{light} time for $\beta = 0.05$ (pink curve), $\beta = 0.1$ (orange curve), $\beta = 0.25$ (red curve), $\beta = 0.5$ (blue curve), $\beta = 0.65$ (green curve), and $\beta = 0.75$ (black curve).

4.3. Suspension Droplets with Variable Particle Size

A set of computations was also performed for particles with uniform density, but two different values of particle radius. For such problems, we must add to the set of dimensionless parameters the relative difference in particle radius $\alpha = |r_{p2} - r_{p1}| / \bar{d}$. In the computations in this section, the value of α is varied and all other parameters are held constant at $\beta = 0$, $\bar{d} / L = 0.04$, $\chi = 1/3$, $N_0 = 300$, $N_1 / N_2 = 1$, and $\text{Re}_d = 10$.

A plot showing a time series of particle positions for a case with $\alpha = 0.41$ is given in Figure 26. It is observed that a tail quickly forms behind the falling droplet, which is primarily formed of the smaller particles. The value of the isolated settling

velocity both for the smaller particles in Figure 26 is smaller than the isolated fall velocity for the nominal particle size. The larger particles, with larger value of the isolated settling velocity, tend to remain inside the falling droplet, although over a long time the larger particles are gradually ejected into the tail, but at a rate much less than the ejection rate of the smaller particles. The shape of the droplet seems to oscillate with time, but at longer times a flattened shape similar to that described by Pignatelli et al. (2011) is observed.

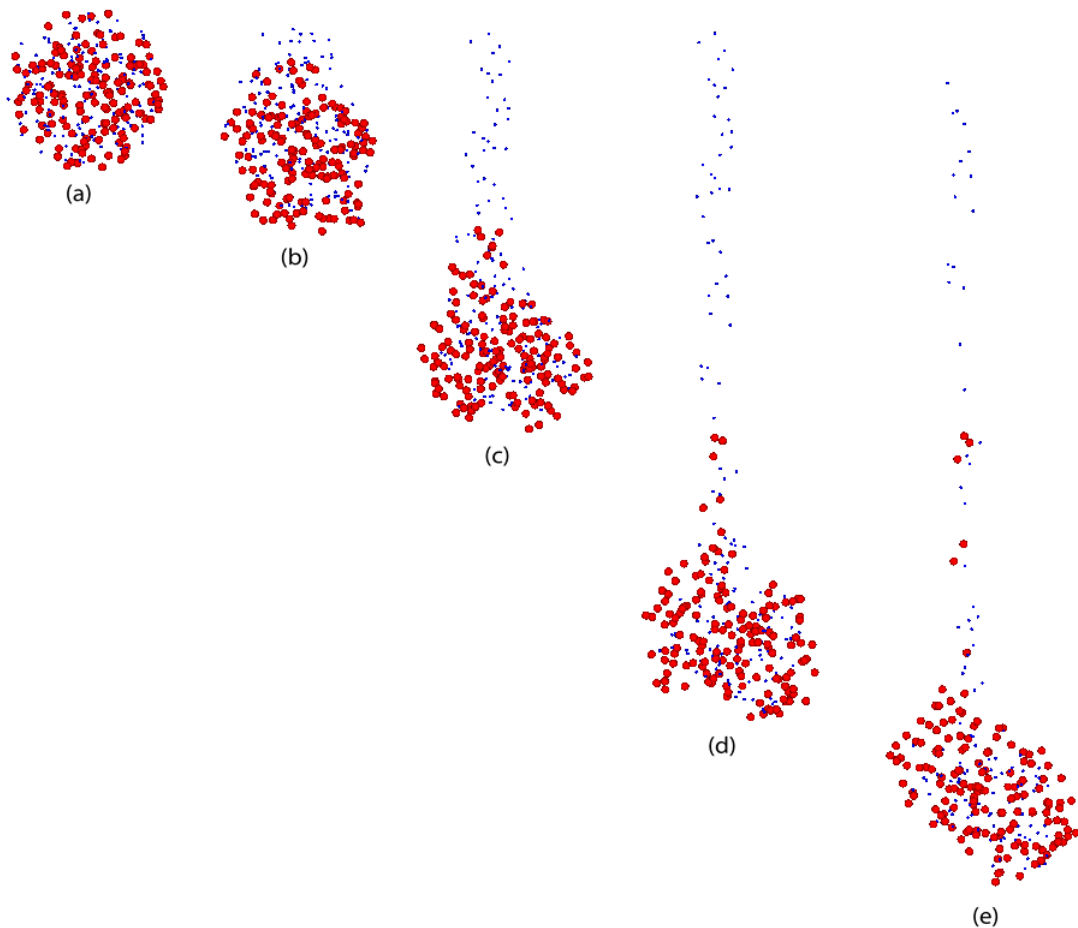


Figure 26: Time series of a falling droplet for a case with two particles sizes with $\alpha = 0.41$, so that $d_1/L = 0.1$ (red) and $d_2/L = 0.026$ (blue), showing preferential

motion of the small particles into the tail. Images are shown at times (a) $t^* = 0$, (b) 0.2, (c) 0.4, (d) 0.6 and (e) 0.8.

The average fall velocity v_{ave}^* is plotted versus time for different values of α in Figure 27a, with $\alpha = 0, 0.14, 0.22, 0.41,$ and 0.57 . Two curves are plotted for each α value, where the value of α is identified by color. The dashed line represents the smaller size particles, and the solid line represents the larger size particles. For small values of α , the average fall velocity is nearly the same for the small and large particles. As α increases, the average fall velocity of the large particles increases and that of the small particles decreases. The droplet fall velocity is plotted with time for different values of α in Figure 27b. The droplet velocity slightly increases with increasing α value due to droplets of larger α values including particles of larger size. The difference in the droplet fall velocity between different α values is greater at earlier times (closer to the peak velocity) and slightly decreases with time. Comparing Figure 28a and Figure 28b, the droplet fall velocity values are similar to the average velocity values of the larger particles, which is consistent to the results for computations with varying β discussed in the previous section. These values are similar because as the droplet falls, the smaller particles enter the tail at a faster rate than the larger particles, so that after sufficient time the droplet is predominately made up of larger particles.

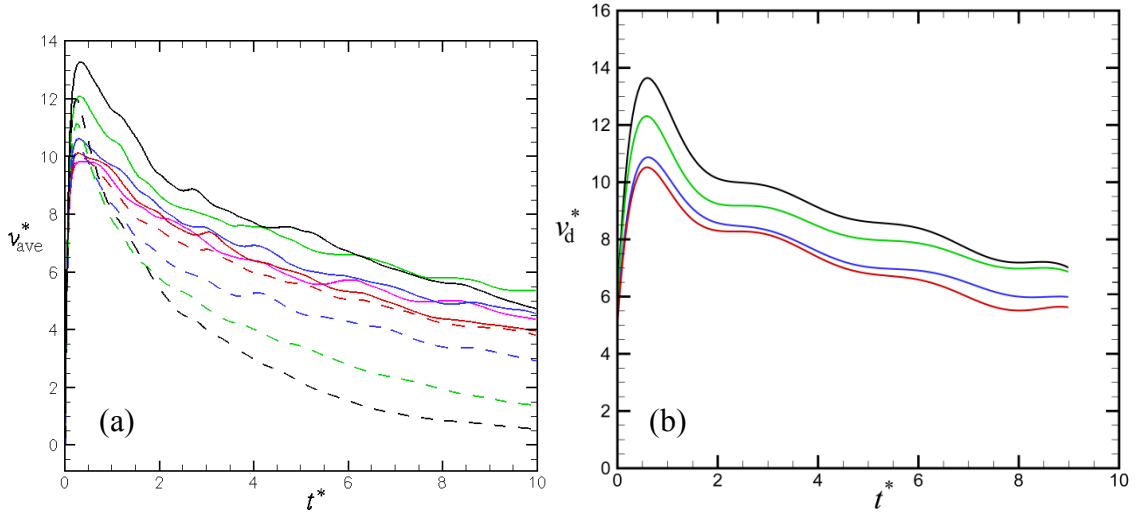


Figure 27: Comparison of the (a) average fall velocity and (b) droplet fall velocity as functions of t^* for $\alpha = 0$ (pink line), 0.14 (red lines), 0.22 (blue lines), 0.41 (green lines), and 0.57 (black lines). In (a), the large particles are indicated using dark lines and the small particles are indicated using dashed lines.

The root-mean-square value y_{rms}^* and the percentage of particles P remaining in the droplet are plotted as functions of time for different values of α in Figure 28. The data is smoothed by plotting the droplet fall velocity with a 9th order polynomial. In Figure 28b, a dimensionless droplet diameter of 1.25 is used again, and any oscillations in the curves are results of variations in droplet shape. The trends observed in the y_{rms}^* and P values for computations with different particle radii are similar to those observed in the computations with different particle densities. For the larger particles, the y_{rms}^* values increase with increasing α values, and correspondingly, the P values for the larger particles seem to decrease with increasing α values, although there is not much spread between the different curves for the larger particles. For the smaller particles, the value of y_{rms}^* is greater for larger α values, corresponding to computations with smaller

particles than for computations with smaller α values. Correspondingly, the P values for the smaller particles decrease with increasing α value, indicating that computations with smaller particles have an increasing tendency for the particles to be removed into the droplet tail as the difference in particle radius is increased. When the value of P approaches zero, all of the small particles have been removed from the droplet and the corresponding value of y_{rms}^* approaches an asymptotic value.

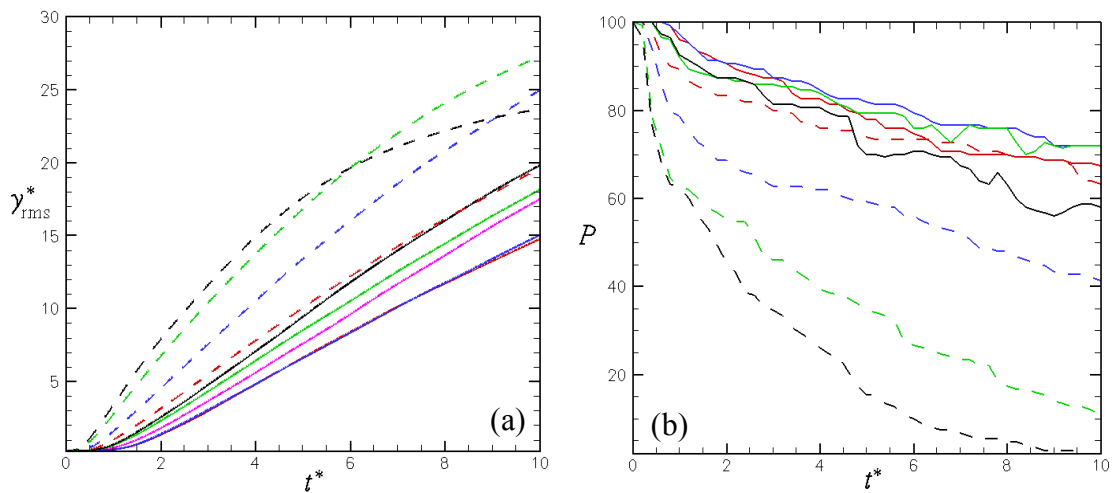


Figure 28: Plot of (a) y_{rms}^* and (b) percentage of particles P remaining in the droplet as a functions of time with different values of α , comparing values for the large particles (solid lines) and for the small particles (dashed lines). The plot uses the same legend as in Figure 27.

The value of the mixing measure defined in (4.4) for the small particles, denoted by G_{small} , is plotted as a function of time in Figure 29 for different values of α . The results are similar to those observed for the computations with different particle density values, only with α taking the place of β . The deviation of the mixing measure from unity, which is a measure of particle segregation, increases as α increases, although there is relatively little difference in the value of G_{small} for the cases with $\alpha = 0.41$ and 0.57 .

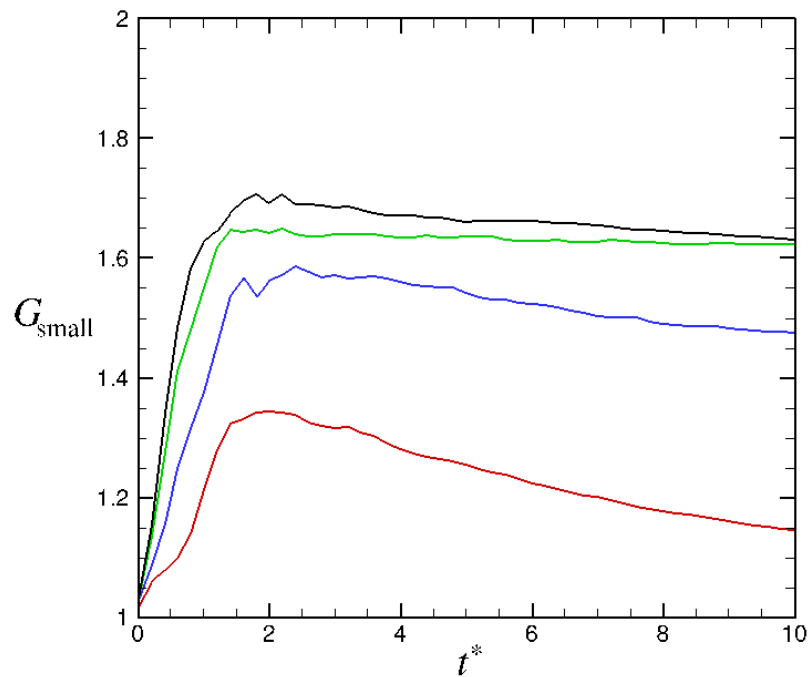


Figure 29: Plot showing time variation of the mixing index G_{small} for $\alpha = 0.14$ (red line), 0.22 (blue line), 0.41 (green line), and 0.57 (black line).

4.4. Suspension Droplets with Size and Density

Distributions

Simulations were performed for cases with a statistical distribution of both particle density and size. These distributions were specified using a Gaussian random variable with mean values $\bar{\rho}_p$ and \bar{d} , respectively, and standard deviation σ , where for convenience the same standard deviation was used for both particle density and diameter. The isolated fall velocity U_n was computed for each particle by

$$U_n^* = \frac{\rho_n}{\bar{\rho}_p} \left(\frac{d_n}{\bar{d}} \right)^2. \quad \text{i)}$$

Simulations were conducted for $\sigma = 0.1, 0.2, 0.3,$ and 0.4 . The results were qualitatively similar for the different cases, although the rate of particle segregation increased with increase in σ . For each run, the particle results were organized into a set of bins by sorting the particles according to the value of the isolated-particle terminal fall velocity U_n for bin n . The number of particles in each bin was specified by $N_{bin} = N_p / N_b$, where N_p is the total number of particles and N_b is the number of bins. The N_{bin} particles with the lowest values of U_n were placed in the first bin, the N_{bin} particles with the next lowest values of U_n were placed in the second bin, and so forth. Mean values of isolated fall velocity U_n for each bin are recorded in Table 1.

Table 1: Average dimensionless fall velocity of an isolated particle (non-dimensionalized by the fall velocity of the nominal particle U) for each of five bins in simulations in which particle size and density are set using a Gaussian random variable with standard deviation σ .

Bin Number	Dimensionless Fall Velocity for Isolated Particles			
	$\sigma = 0.1$	$\sigma = 0.2$	$\sigma = 0.3$	$\sigma = 0.4$
1	0.701	0.459	0.308	0.215
2	0.859	0.719	0.591	0.536
3	0.958	0.907	0.853	0.879
4	1.083	1.156	1.276	1.417
5	1.305	1.654	2.040	2.443

Diagnostics were computed separately for each bin as a function of time, including average y -position y_{ave} , average fall velocity v_{ave} , root-mean-square y -position y_{rms} , and percentage of particles P from that bin remaining in the droplet. Plots of these different measures are plotted in Figure 30 and Figure 31 for the case with $\sigma = 0.4$. It is observed in Figure 30 that while all particles have about the same peak velocity shortly after release of the droplet, the light/small particles decrease their velocity faster as time progresses compared to the heavy/large particles. For bins 3-5, the value of y_{rms} is observed in Figure 31a to decrease with fall velocity of the particles (i.e., with bin number). This observation is consistent with the observation that the larger and heavier particles tend to remain in the suspension droplet whereas the lighter and smaller particles tend to be transported into the tail. The value of y_{rms} for bins 1-3 is very similar for $t^* < 3$, but eventually the value of y_{rms} flattens out and decreases below that of bins 2 and 3. This occurs because the particles in bin 1 are quickly transported into the tail, so that after some time all of the bin 1 particles are in the tail and the value of y_{rms} attains a

nearly constant value. The largest values of y_{rms} occur for particles of intermediate value of fall velocity, which enter into the tail but also remain in the drop for sufficient time periods that they are distributed over larger distances in the y -direction.

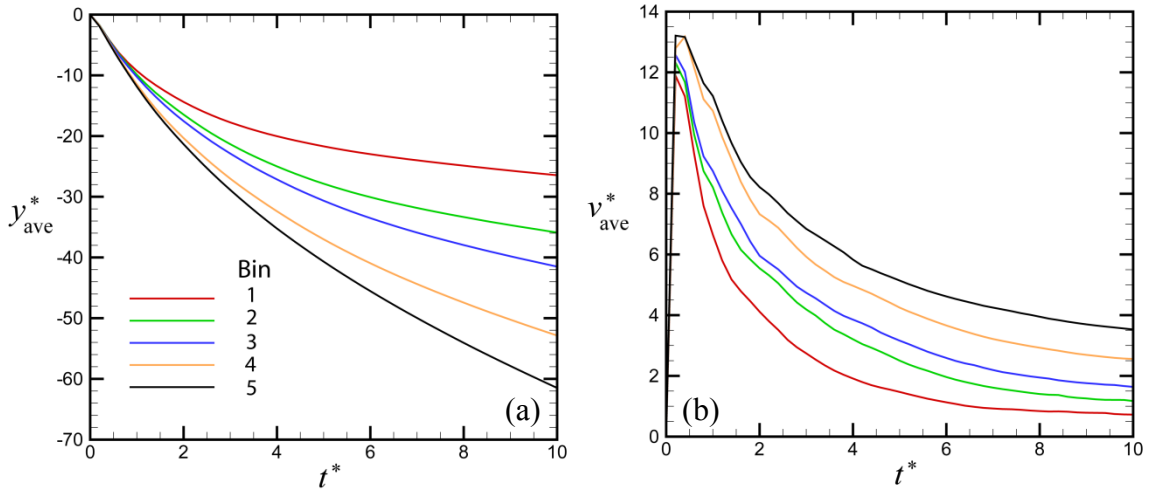


Figure 30: Time variation of (a) y_{ave}^* and (b) $v_{ave}^* = -dy_{ave}^* / dt^*$ for five different bins in a simulation with a distribution of particle size and density having standard deviation $\sigma = 0.4$. Figure (b) uses the same legend as in (a).

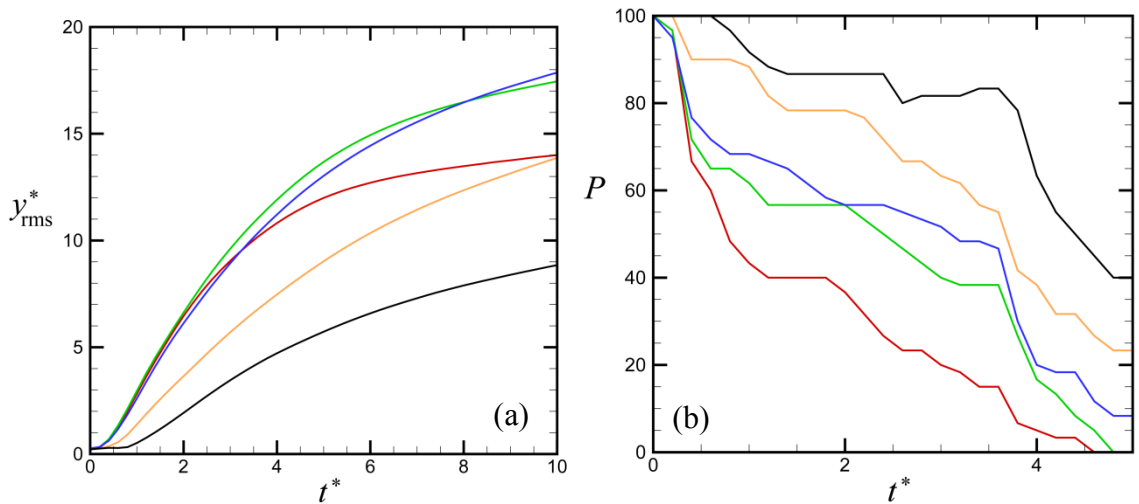


Figure 31: Time variation of (a) y_{rms}^* and (b) percentage of particles within the bin remaining in the droplet for five different bins in a simulation with a distribution of particle size and density having standard deviation $\sigma = 0.4$. The plots use the same legend as in Figure 30a.

The percentage P_n of particles in bin n that remain in the droplet is plotted as a function of time in Figure 31b. This plot quantifies how particles with small values of the isolated settling velocity U_n preferentially segregate into the tail region, with the rate of segregation being faster for particles with smallest values of U_n . A rapid decrease in P_n is observed near $t^* = 4$, which is associated with the growth and deformation of the droplet. To understand this latter effect, scatter plots of the particle positions within the droplet and the region of the tail nearest the droplet are shown at four times in Figure 32. The droplet initially falls with a roughly spherical shape (Figure 32a), with a tail consisting mostly of the light/small particles. With time the droplet shape deforms into a toroidal shape (Figure 32b) and more of the heavier/larger particles pass into the tail. At around $t^* = 4$, the droplet grows in size and becomes increasingly disorganized (Figure 32c). By $t^* = 5$, there isn't a recognizable droplet but instead the particles are scattered widely and have little hydrodynamic interaction with each other (Figure 32d).

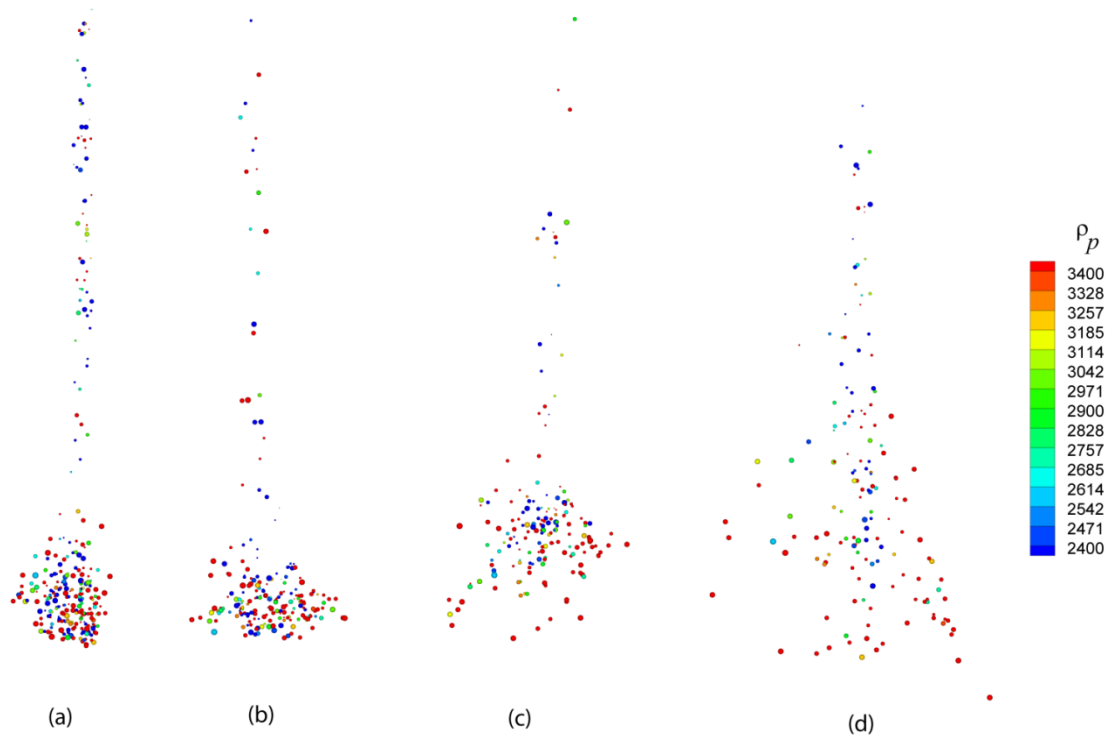


Figure 32: Plot showing a scatter diagram of the droplet and the near section of the tail for the case with distributed particle size and density with $\sigma = 0.4$, at times (a) $t = 1$, (b) 2, (c) 4, and (d) 5. The scatter size shown is proportional to the particle diameter, and the particle density is indicated by color as given by the legend on the right (in kg/m^3).

4.5. Mechanisms of Preferential Leakage of Light/Small Particles into the Droplet Tail

In each of the cases discussed in Section 2, the motion of the particles into the droplet tail follows a series of three stages, which are illustrated in the computational results shown in Figure 33. In the first stage (Figure 33a), occurring shortly after release of the droplet, a large number of the lighter and smaller particles are rapidly swept into the droplet tail, with most of the heavier and larger particles remaining in the droplet. In

the second stage (Figure 33b), the rate of particle motion into the droplet decreases, and the particles entering into the tail consist of a mixture of particles of all sizes and densities. However, there is still a higher proportion of light/small particles entering the tail than heavy/large particles in this stage. In the third stage (Figure 33c), the light/small particles have nearly all passed into the tail, and the remaining heavy/large particles gradually trickle into the tail.

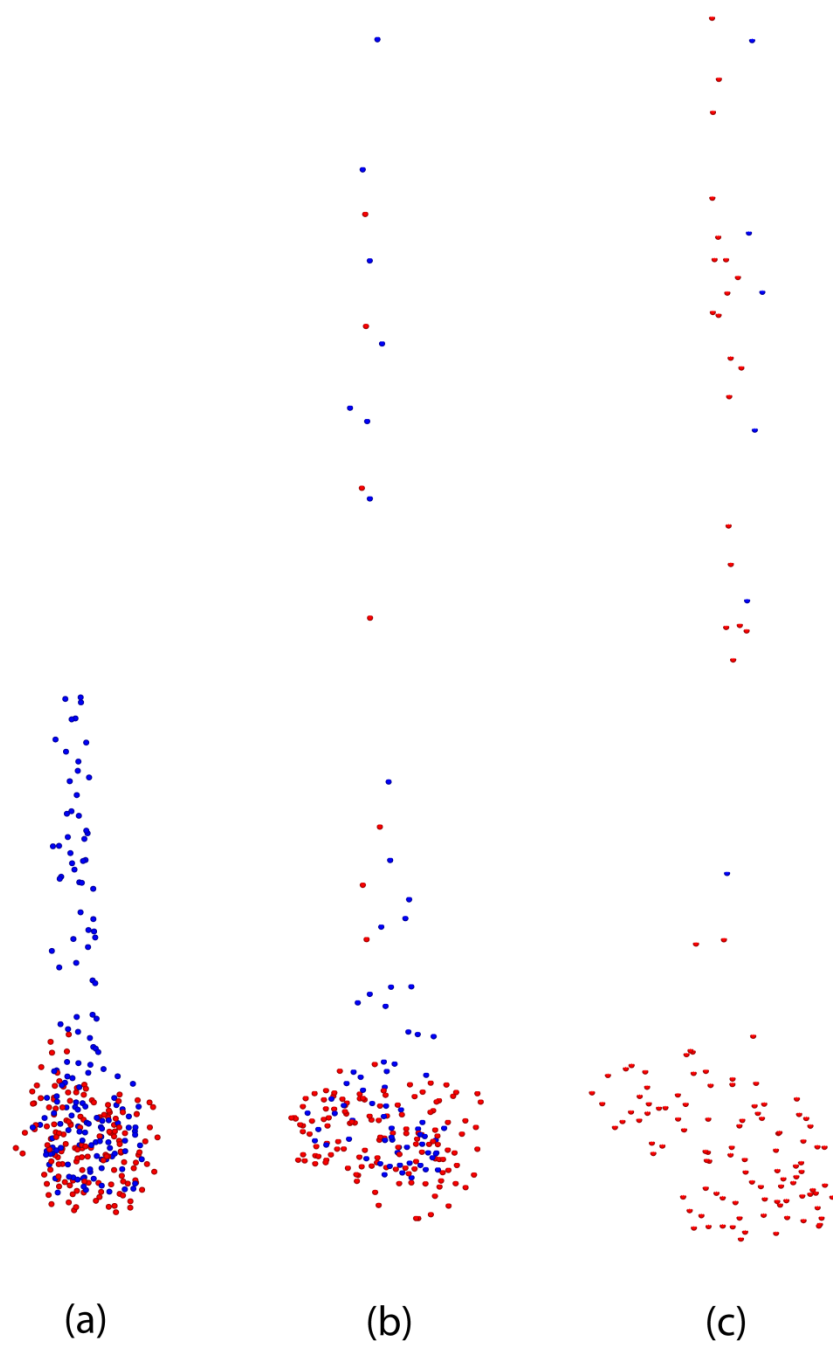


Figure 33: Plot showing particle locations for a computation with two densities and $\beta = 0.5$, showing times characteristic of tail formation stages: (a) Stage 1 ($t^* = 0.6$), (b) Stage 2 ($t^* = 3.0$), (c) Stage 3 ($t^* = 10.0$).

In order to discuss the mechanisms giving rise to these three stages, a schematic diagram showing fluid streamlines (on the left) and particle pathlines (on the right) in a frame moving with the suspension droplet is given in Figure 34. The particles settle downward due to gravity and thus slip relative to the local fluid velocity at a rate approximately equal to the isolated particle settling velocity U_n . As noted by Nitsche and Batchelor (1997), the presence of particle slip relative to the fluid leads to penetration of the fluid streamlines into the outer region of the droplet, indicated by Region II in Figure 34. This streamline penetration leads to formation of an effective no-penetration boundary in the droplet interior, indicated by a heavy dashed line in Figure 34. Inside this boundary is denoted as Region I in Figure 34, whereas outside the droplet is denoted as Region III. As a consequence of the fluid penetration, when the outer particles within the droplet approach the rear of the droplet (identified as the tail formation region in Figure 34), they experience an upward fluid velocity, pulling them away from the droplet and into the droplet tail, which is counter to the downward settling velocity of the particles.

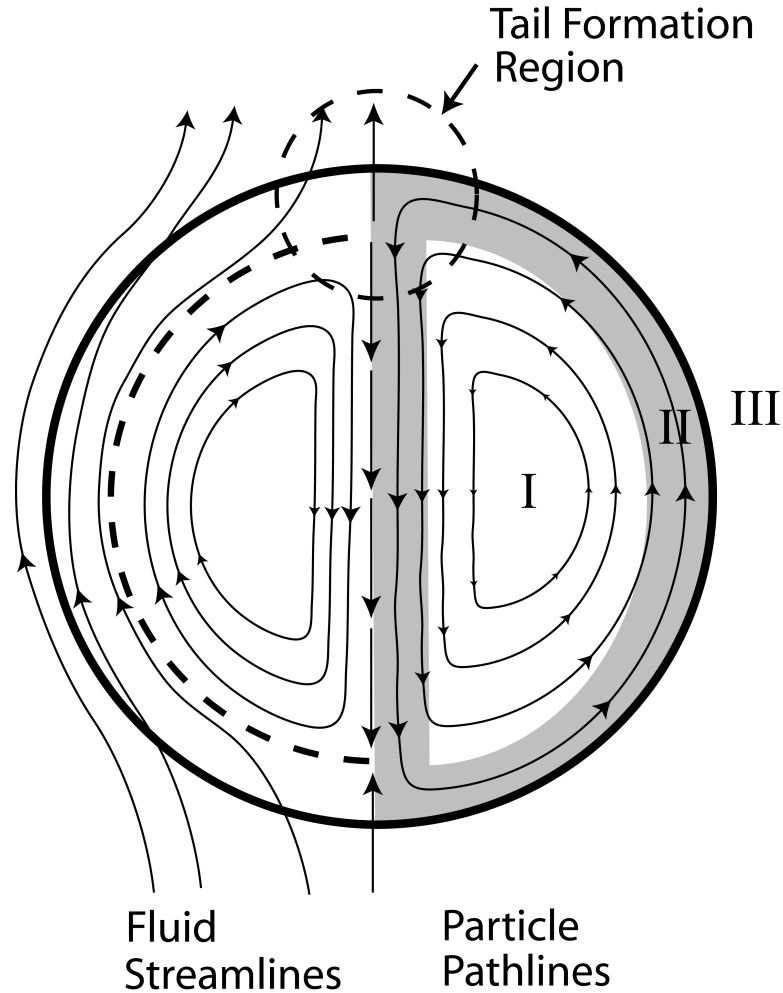


Figure 34: Schematic diagram showing fluid streamlines (on the left) and particle pathlines (on the right) in a frame moving with the suspension droplet. Due to downward particle slip relative to the fluid, the fluid streamlines penetrate the outer part of the droplet giving an effective droplet boundary (dashed line on the left) that has smaller radius than the droplet. Particles in Region I are within the no-penetration surface so the fluid flow is always in the direction of particle motion, whereas particles in Region II (shaded grey) experience fluid flow counter to the direction of particle motion when they pass through the tail formation region (indicated by a dashed circle). Region III denotes the exterior of the droplet.

The first stage of tail formation occurs shortly after release of the droplet. This stage involves particles in the annular region shaded in grey in Figure 34, which pass through Region II as they are advected around by the swirling flow within the droplet. As

these particles enter into the tail formation region, they experience a fluid flow that is in the opposite direction from the direction of particle motion. Particles whose slip velocity due to gravity (approximately given by the particle isolated fall velocity U_n) is greater than the fall velocity U of the nominal particle settle downward back into the droplet, returning to the rotating swirling motion within the droplet. However, particles with isolated fall velocity less than U do not have sufficient downward velocity to oppose the fluid flow, and these particles are thus swept by the fluid velocity into the droplet tail. The first stage of tail formation is complete when the light/small particles (with $U_n < U$) within this annular grey-shaded region have all been removed from the droplet.

The second stage of tail formation occurs due to collisions between particles, which give rise to a random motion that must be added to the particle velocity field induced by the fluid drag and reduced gravitational force. In some cases, these random motions will cause light/small particles to drift from the inner part of the droplet (Region I) into the outer part of the droplet (Region II), wherein they are eventually swept into the tail when they enter the tail formation region shown in Figure 34. These random motions also cause heavier/larger particles to drift across the droplet outer boundary from Region II to the exterior Region III, wherein they are swept into the droplet tail by the fluid flow. Because these random motions are essentially diffusive in nature and affect all particles, the second phase of tail formation occurs more slowly than the first phase and includes particles of all sizes and densities. However, since the particle concentration is greater within the inner part of the droplet (Region I) than within the outer part (Region II), and also because light/small particles tend to receive a greater rebound velocity upon collision

compared to heavy/large particles, the light/small particles have a greater likelihood to be removed into the droplet tail during this stage than do the heavy/large particles.

In the third stage of tail formation, all of the light/small particles have been removed from the droplet and are scattered throughout the droplet tail. Consequently, in this stage only the heavy/large particles remain in the droplet and the tail formation occurs by the same process discussed by Nitsche and Batchelor (1997) for a uniform particle size and density. As in the second stage discussed above, this process consists of random motions due to particle collisions causing particles to move outside of the droplet boundary, from Region II to Region III.

Chapter 5

Experimental Investigation

5.1. Experimental Method

A series of experiments were conducted in which a particle suspension droplet settles in a container filled with a transparent fluid. A diagram of the experimental set-up is given in Figure 35. The vessel used in the experiments has inner cross sectional dimensions of 9 cm by 9 cm, and was filled to a height of 28 cm. The vessel was filled with a mixture of water-soluble UCONN oil and water to create a fluid with a viscosity of 174 cSt. The container was lit from the side with white light from four 6400K fluorescent tubes. A ruler with millimeter scale spanning the container height was attached to the other side, and the container was placed in front of a black background. The video camera used to capture the images of the falling droplet was a Sony HDR-SR12 with a frame rate of 30 frames per second.

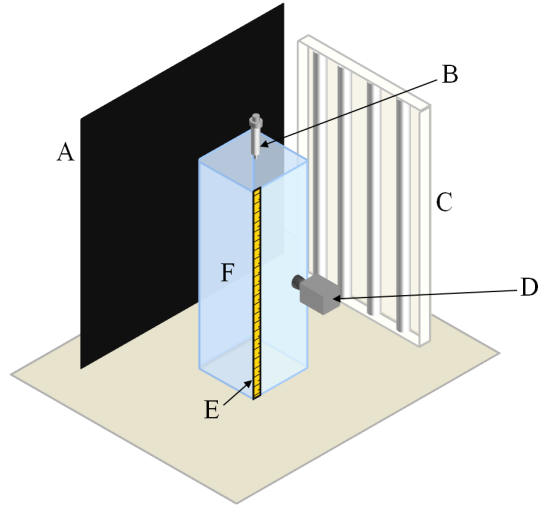


Figure 35: Diagram of the experimental set-up including (A) the black background, (B) the injection syringe, (C) the lighting system, (D) the video camera, (E) the ruler, and (F) the vessel.

Combinations of four different types of spherical particles were used in the experiments, the characteristics of which are given in Table 2. The particle size distributions were calculated with a digital imaging system (Image Pro Plus 6.0, Media Cybernetics), where the diameter given in the table is the mean diameter and the error stated is equal to one standard deviation, with sample sizes between 70 and 100 particles. The particle density was calculated by measuring the mass of a sample of particles and dividing it by the measured volume of the same sample. The mass was measured with a scale that has a precision of ± 0.0001 grams, and the volume was measured by putting the sample into a graduated cylinder with a 0.2ml scale and adding a known volume of water into the graduated cylinder. The error in the density value that is given is calculated using the standard error propagation equation from the known uncertainty of the mass and volume measurements. To calculate the terminal settling velocity of each particle, position and time data are taken from a series of time-stamped photos pulled from a video

of the falling particle, with a time precision of ± 0.03 s and a length precision of ± 1 mm. The average particle velocity is calculated by averaging the velocity from 20 samples, and the uncertainty is equal to one standard deviation from the mean.

Table 2: Characteristics of particles used in the experiments.

Particle Label	Material	Color	Diameter (mm)	Density (g/cm^3)	U_p (mm/s)
A	Glass	Gold	0.36 ± 0.03	2.44 ± 0.1	0.39 ± 0.1
B	Glass	Red	0.78 ± 0.05	2.55 ± 0.16	1.7 ± 0.3
C	Aluminum	Silver	0.77 ± 0.01	2.86 ± 0.35	2.1 ± 0.1
D	Chrome steel	Silver	0.96 ± 0.01	8.94 ± 1.9	13.0 ± 0.2

The particle suspension was formed by first measuring out the two sets of particles to be used in the given experiment. The particle number ratio N_1 / N_2 for all of the experiments was set equal to 1. To allow for an equal number of particles of each particle type to be measured out, tweezers were used to count out 100 particles of each particle type, and the mass of the 100 particles was recorded with an accuracy of ± 0.0001 grams. Using these values, the number of particles in a sample was obtained by measuring the sample's mass. Once an equal number of particles of each type were measured, both sets of particles were put in a small closable container and the container was vigorously shaken. The particles were then put into a syringe with a 4mm diameter opening and, with the syringe extended to leave empty space for mixing, the syringe was vigorously shaken to ensure that the particles in suspension were well mixed. Fluid from

the vessel was then added to the particles in the syringe, and the syringe was vigorously shaken again to ensure an even distribution of the two types of particles within the suspension. The particle suspension was injected into the fluid in the test vessel by holding the syringe vertically with the syringe tip about 1cm above the surface of the fluid. The suspension was manually injected into the container by applying slight pressure to the syringe causing a droplet that is attached to the syringe to slowly form. The droplet falls into the fluid when the weight of the droplet exceeds the surface tension force between the droplet and the syringe. The suspension droplets used in the experiments have higher concentration values than those used in the computations. The experimental concentration is higher due to larger particle sizes, and due to the particles having a higher density than the fluid. Because the particles were denser than the fluid, it was not possible to keep them from slightly settling out of the liquid while in the syringe, and making the droplet more concentrated than the original solution in the syringe.

The number of particles in the suspension droplet was estimated by measuring the mass of a series of droplets that were dripped onto a surface, using the same approach for droplet generation as used in the experiments. Sample sizes of 21, 20 and 28 were used for experiment sets 1, 2, and 3 respectively. The known droplet concentration was then used to calculate the approximate number of each type of particle in each sample droplet. The average number of each type of particle in a droplet and the associated root-mean square uncertainty were computed from the sample, with values listed in Table 3. Each droplet consisted of approximately even amounts of N_1 and N_2 .

Table 3: Parameters characterizing the experimental data sets.

Set #	Particles in Suspension	β	α	Avg. L (mm)	Avg. Re_d	$\bar{\rho}_p$ (g/cm^3)	\bar{d} (mm)	Avg. N_0
1	A & B	0.022	1.43	4.1	0.69	2.495	0.61	156±18
2	B & C	0.057	0.02	4.2	0.87	2.705	0.775	85±10
3	B & D	0.556	0.24	3.7	1.94	5.75	0.87	44±9

5.2. Experimental Results

Experimental runs were first performed in a vessel filled with a lower viscosity fluid to examine the evolution of a suspension droplet with much lower particle concentration. The lower viscosity fluid allowed for the falling particles to spread out more with the initial impact and form a suspension droplet with a much lower initial concentration. Similar to what was observed in the computations with low particle concentrations shown in Figure 21, the two types of particles immediately start to separate from each other and there is no droplet tail formation. Because the particles are spread out from each other, there is significantly less hydrodynamic interaction of the falling particles, which is the driving mechanism for the tail formation.

Since we are primarily interested in particle segregation in cases with large amounts of hydrodynamic interaction of the particles, the primary focus of the experiments was on cases with sufficiently large particle concentration that the entire particle set settles downward as a single droplet, with the exception of the thin tail that

trails behind the droplet. Four sets of experiments were performed, with multiple runs performed for each set. The characteristics of each set are listed in Table 3. In experiment set 1, the particles have the same density but different particle radii. In experiment set 2, the particles have nearly the same radius, but different densities. In experiment set 3, both the particle radius and density are different. The average d_d and Re_d were averaged from 5, 9, and 8 runs for experimental set numbers 1, 2, and 3 respectively.

In some of the experimental runs, the droplet was initially teardrop shaped instead of spherical, as a result of its injection into the fluid in the vessel. In such cases, the particles that enter the fluid last are the ones contained in the rear of the tear drop, and are observed to quickly break apart from the droplet, leaving a roughly spherical droplet composed of the remaining particles. All of the experimental analysis starts with the droplet in this spherical shape, and does not include the particles that were contained in the initial tail of the teardrop.

Runs with experimental set 1 were conducted to study the problem of a falling suspension droplet containing two different size particles, with $\alpha = 1.43$. Figure 36 shows a time series of photos of a set 1 suspension droplet falling, where the large particles (red) are about 2.2 times larger than the small particles (gold). The tail that forms behind the droplet consists of both small and large particle sizes, but the small particles are more numerous in the tail region than the large particles. Runs with experimental set 2, shown in Figure 37, were conducted to study the problem of a falling suspension droplet containing two different density particles, with $\beta = 0.067$. The heavy particles (silver) are 14% heavier than the light particles (red). The droplet tail contains

both heavy and light particles, but the light particles are significantly more numerous. Experimental set 3, shown in Figure 38, compares particles with a substantial difference in both particle size and density, with $\alpha = 0.44$ and $\beta = 0.473$. The tail behind the droplet consists of only smaller/lighter particles for the majority of the time, until at a later time one larger/heavier particle eventually enters the tail.



Figure 36: Photo of the particle positions of a falling droplet, with initial droplet diameter $d_d = 3.8$ mm, in experimental set 1 at times (seconds): (a) $t = 0$, (b) $t = 0.8$, (c) $t = 1.8$, (d) $t = 3.8$, and (e) $t = 4.3$. The large particles (red) are about 2.2 times larger than the small particles (gold).

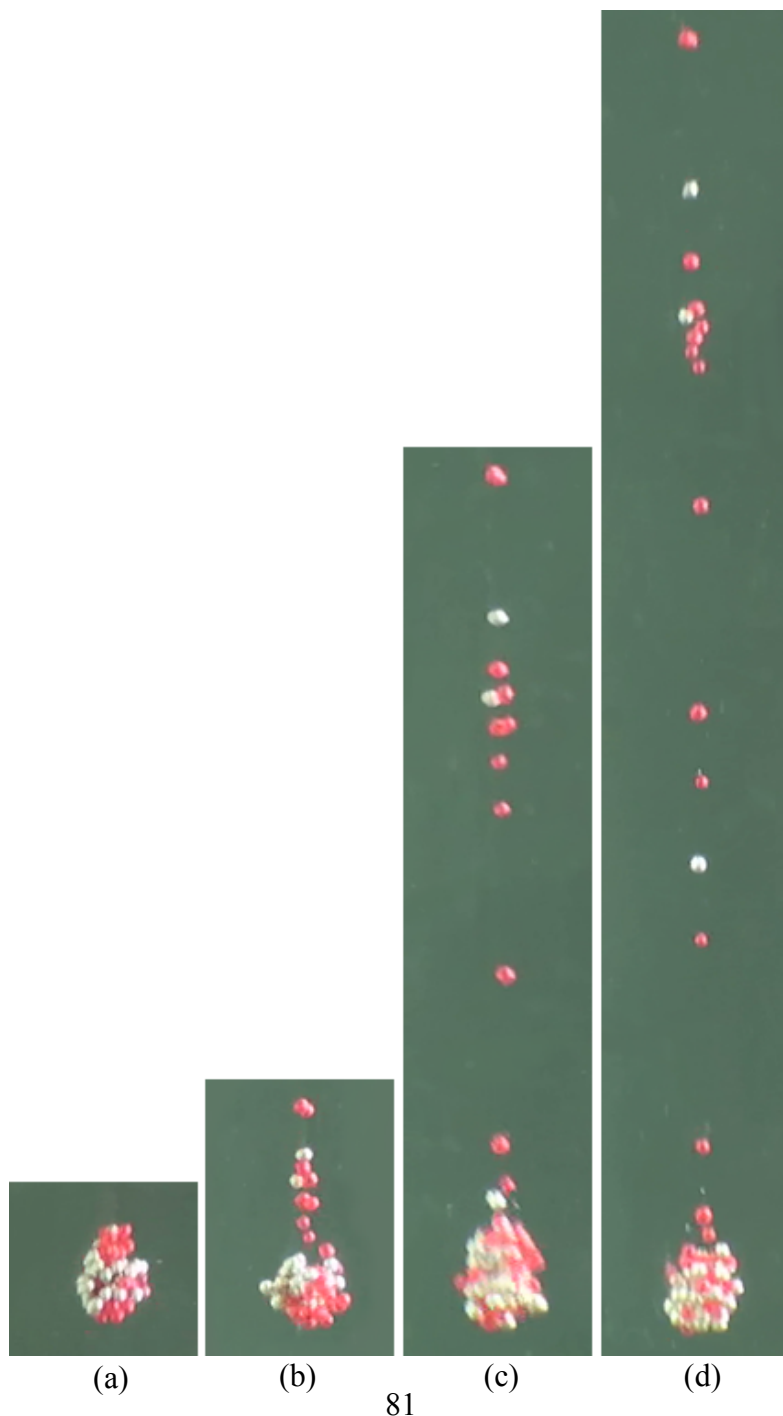


Figure 37: Photo of the particle positions of a falling droplet with initial droplet diameter $d_d = 4\text{ mm}$ in experimental set 2 at times (seconds): (a) $t = 0$, (b) $t = 1.2$, (c) $t = 2.7$, and (d) $t = 4.2$. The heavy particles (silver) are 14% heavier than the light particles (red).

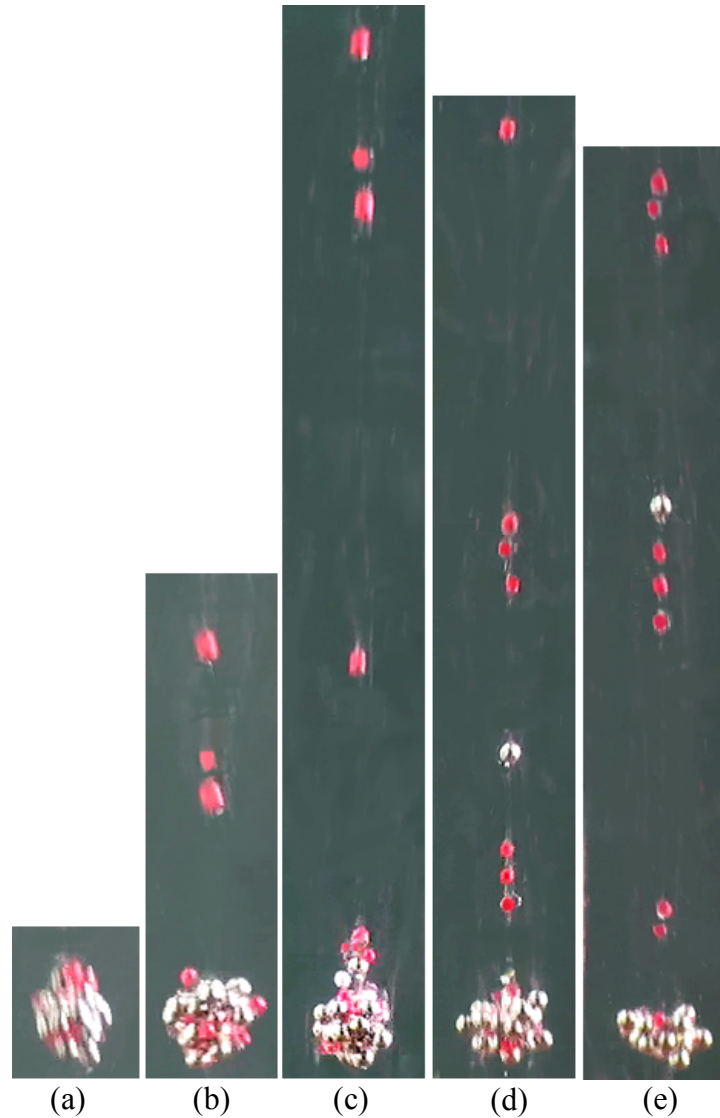


Figure 38: Photo of the particle positions of a falling droplet with initial; droplet diameter initial $d_d = 3.5\text{ mm}$ in experimental set 3 at times (seconds): (a) $t = 0$, (b) $t = 0.44$, (c) $t = 0.94$, (d) $t = 1.4$, and (e) $t = 1.74$. The large/heavy particles (silver) are 27% larger and 3.2 times heavier than the small/light particles (red).

Plots of the droplet fall velocity with time are created from the experimental results and are shown in Figure 39 a-c for experiment sets 1-3. To calculate the velocity, position and time data are taken from a series of time-stamped photos pulled from a video of the falling suspension droplet, with a time precision of ± 0.03 s and a length precision of ± 1 mm. The uncertainty of the experimental droplet fall velocity is computed using the standard propagation of error equation from the measured uncertainty in the change in particle distance and the change in time, and is found to be ± 0.99 mm/s, ± 0.99 mm/s, and ± 8.7 mm/s for sets 1, 2, and 3 respectively. The droplet velocity decreases with time, as was also observed in the computations, due to the loss of particles from the droplet as they migrate into the tail. Comparing the velocity magnitudes in Figure 39 b and c, it is noted that the particles with greater mean density (set 3) has a greater fall velocity than the particles with lower mean density (set 2), as would be expected.

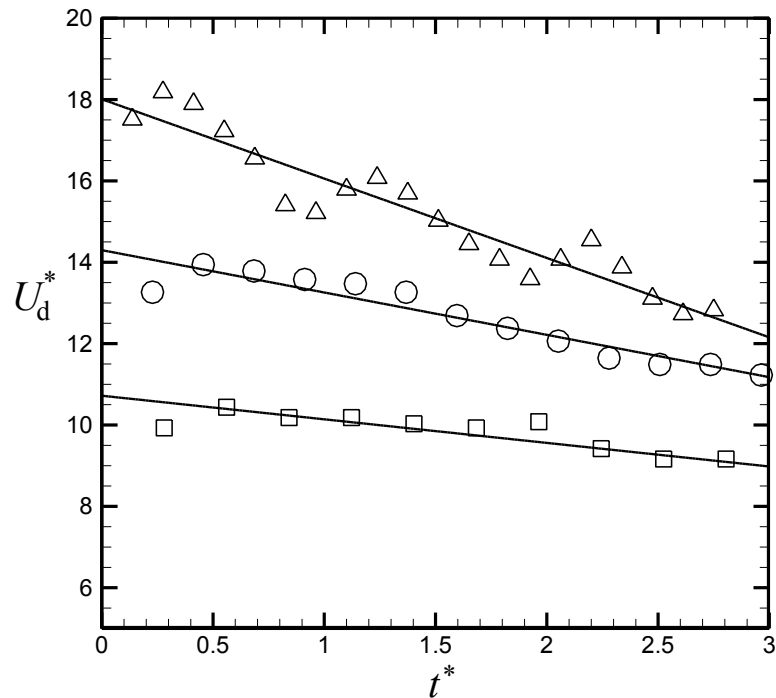
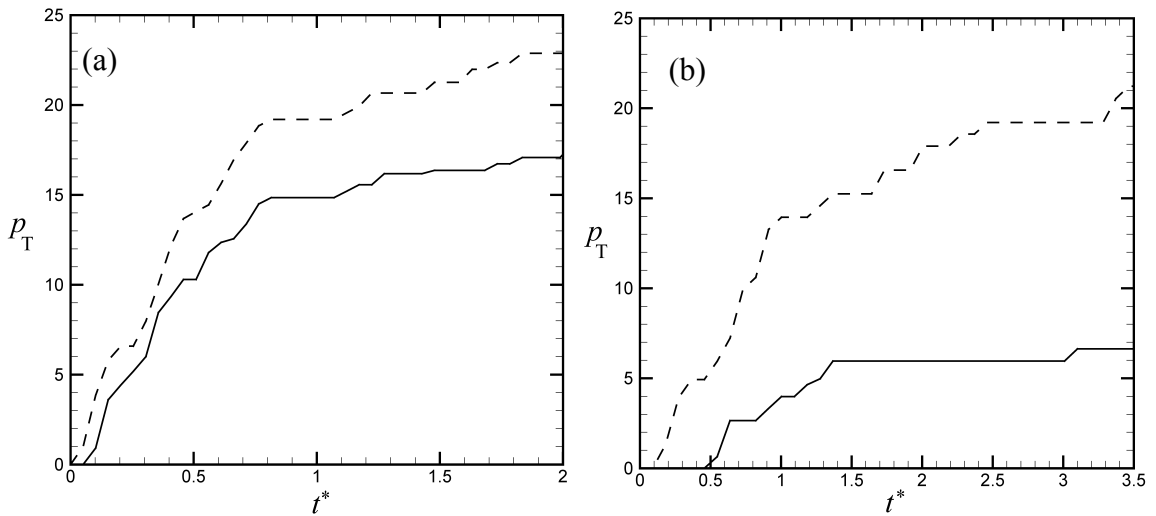


Figure 39: Experimental droplet fall velocity versus time: (a) experimental set 1 (triangles), (b) set 2 (circles), (c) set 3 (squares).

The percentage of each particle type that is contained in the tail was calculated as a function of time, and is plotted in Figure 40a-c for all of the experiment sets. A particle is considered to be part of the tail when there is a visual gap between the particle and the droplet, or when a particle is vertically above the droplet and is connected to the droplet through one particle that is also vertically above the droplet. The percentage is calculated using the average total number of particles in a droplet, and it is assumed that each type of particle makes up exactly half of the total. The error in the time is ± 0.03 s, and the uncertainty in the particle count is ± 1 particle due to human error. The experimental values varied significantly between different runs from the same experimental set due to variation in the initialization of the droplets. The mean values are plotted in Figure 40a-c.

Standard deviation of these values are recorded as 3.0 for the dashed line and 5.5 for the solid line in figure 40a, 6.4 for the dashed line and 3.1 for the solid line in figure 40b, and 10.3 for the dashed line and 1.5 for the solid line in figure 40c. It can be observed that in general, in all of the experimental sets the lighter/smaller particles were the dominant particles in the tail, and the percentage of larger/heavier particles in the tail decreases with increasing β value. Similar variation between runs of the same set also occurred in the experiments of Metzger et al. (2007). Despite the variation, it is important to note the main point observed in all sets, that the lighter/smaller particles are dominant in the tail.



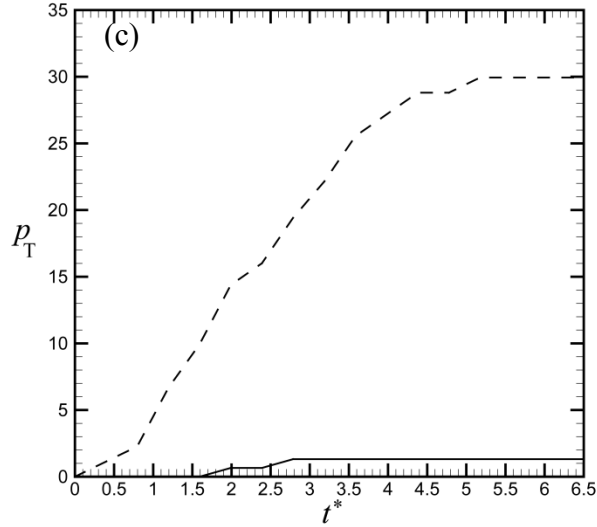
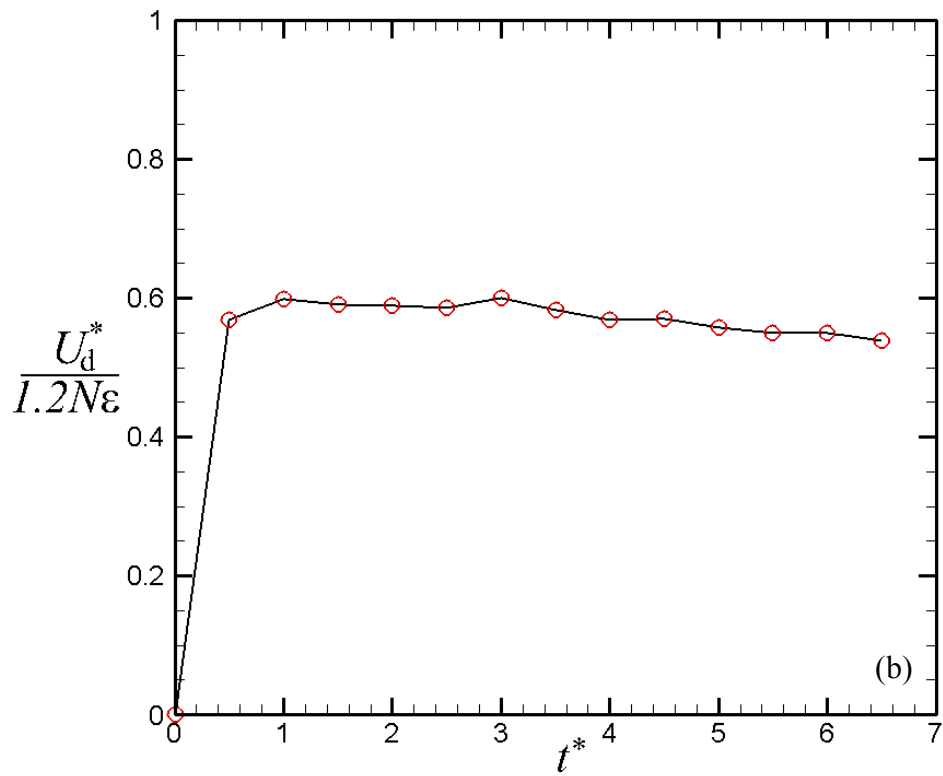
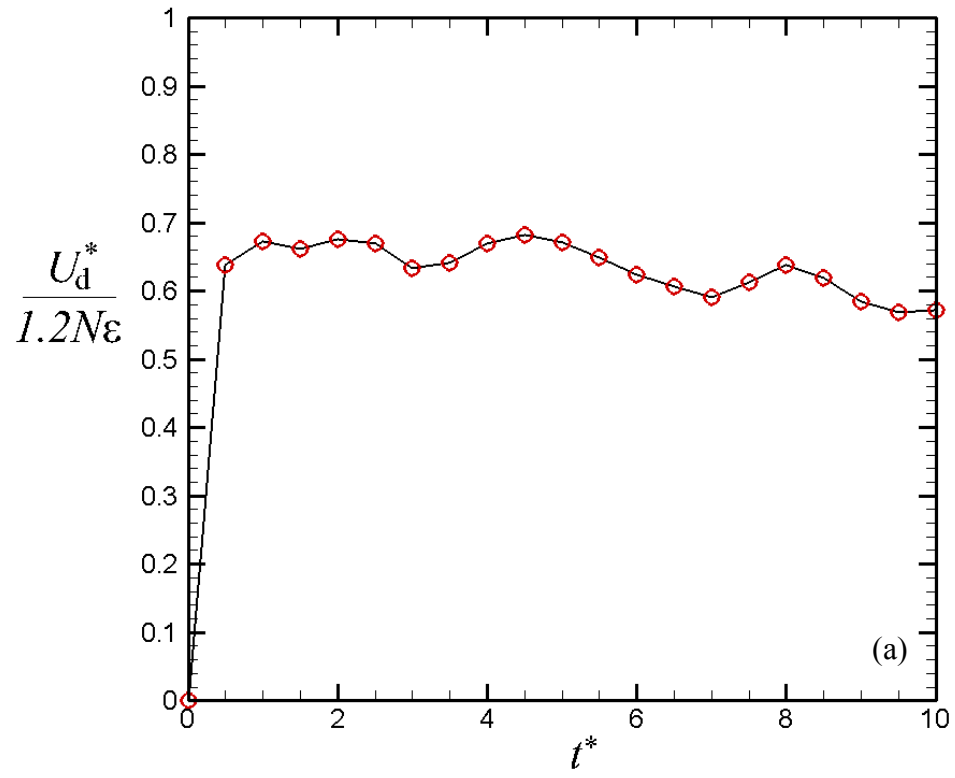


Figure 40: Plots showing the percentage of each type of particle contained in the vertical tail with time, out of the total number of each type of particle for (a) experimental set 1, (b) set 2, and (c) set 3. Solid lines represent heavier (or larger) particles and dashed lines represent lighter (or smaller) particles.

The experimental droplet fall velocity was divided by the theoretical solution (2.9) for one run of each set and is plotted with time in Figure 41a-c. To non-dimensionalize the droplet fall velocity that is used in (2.9), the droplet fall velocity is divided by the experimental terminal settling speed of an isolated particle calculated by averaging the terminal fall velocities of the particles in the set given in Table 2. The droplet diameter is measured with digital imaging software and has an error of ± 1 mm. The number of particles in the droplet with time is calculated by subtracting the number of particles counted in the tail at that time from the initial number of particles in the droplet. The uncertainty of the experimental droplet fall velocity divided by the theoretical solution (2.9) is computed using the standard propagation of error equation from the measured uncertainty in the droplet fall velocity, the particle fall velocity and the number of particles, and is found to be ± 0.16 , ± 0.03 , and ± 0.25 , for sets 1, 2, and

3 respectively. Figure 41a shows that the value of the experimental droplet fall velocity divided by the theoretical solution remains approximately constant with time at values around 0.65, 0.60, and 0.85 for sets 1, 2, and 3 respectively. This behavior is similar to the computational results shown in Figure 19b. The values of Figure 41a and b are very close to those in the simulations, and the values of Figure 41c are only slightly higher than the computational results.



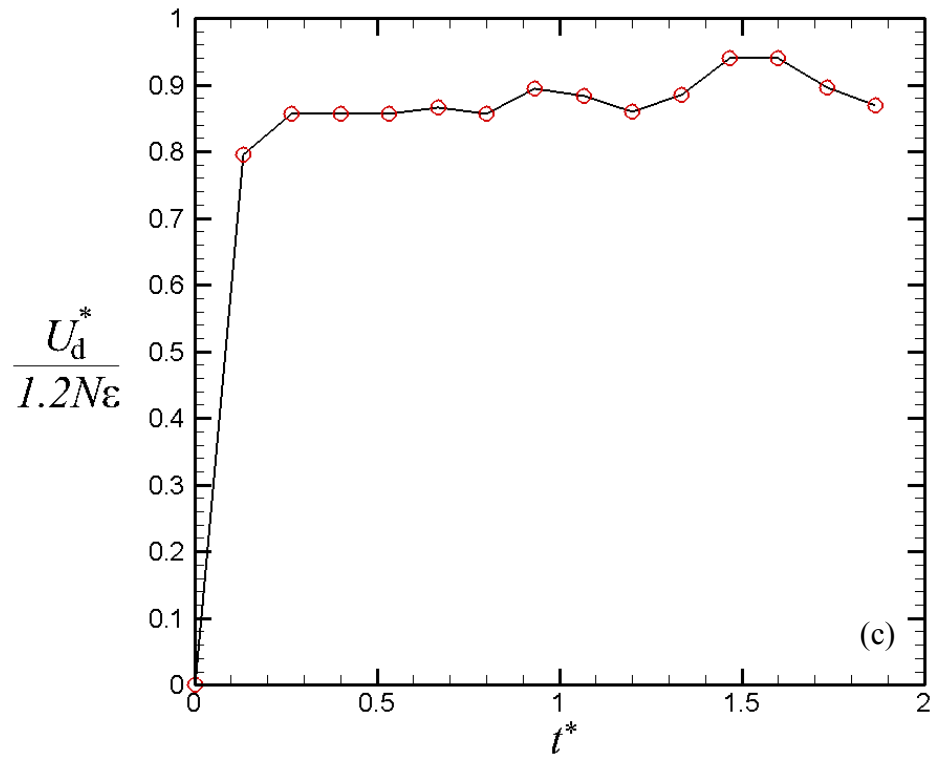


Figure 41: Experimental droplet fall velocity divided by solution to (2.9) plotted with time. (a) experimental set 1, (b) experimental set 2, (c) experimental set 3.

Chapter 6

Conclusions and Future Work

An investigation of segregation of particles of different sizes and densities in a settling suspension droplet was performed using both computations and experiments. The computations approximated the particle hydrodynamic interaction using *Oseen dynamics* – a variation of the Stokesian dynamics method that employs the full Oseen solution to allow finite (non-small) values of the flow Reynolds number, while still requiring that the particle Reynolds number is small. The particle transport and collisions were handled using a soft-sphere discrete element method. The experiments were conducted by observing the fall of suspension droplets formed of binary particle mixtures consisting of particles with different sizes and densities in a viscous fluid.

The particle hydrodynamic interactions are of primary importance for the flow of concentrated suspension droplets, since the droplet settling speed is approximately an order of magnitude larger than that of an isolated particle. Consequently, the ability to accurately predict the suspension droplet dynamics in this flow field is an important test of the Oseen dynamics method. The computed fall velocity of the suspension droplet was compared against an approximate theoretical solution, and the ratio of the computed to

the theoretical values of droplet fall velocity are found to be consistent with both experimental results from our study and with experimental and computational solutions obtained by other investigators. It is observed that dynamics of binary suspension droplets with two different particle types depends on the particle concentration. For low concentrations, the amount of particle hydrodynamic interaction is insufficient to oppose the gravitational separation of the particles, and the particle type with larger isolated particle settling velocity quickly pulls away from the slower particles, leaving a deformed cloud of the slower particles behind. On the other hand, when the particle concentration is sufficiently large, the particle hydrodynamic interaction is sufficient to hold particles of both types together within the suspension droplet, thus inhibiting particle separation and allowing the droplet to settle as a single unit.

The current study provides a detailed examination of suspension droplet dynamics under conditions where strong particle hydrodynamic interaction holds the particle mixture together into one suspension droplet. As was observed also for suspension droplets with uniform particle characteristics, a falling suspension droplet with high concentration develops a thin tail of trailing particles which slowly leak out from the droplet. A novel segregation mechanism is observed to occur, by which the particles with smaller isolated settling velocity have a preferential tendency to be transported into the droplet tail, whereas particles with higher isolated settling velocity have a higher tendency to remain within the suspension droplet. Three different stages of particle segregation are observed – the first in which only the slower particles are transported into the tail, the second with a mixture of particles of different sizes transported into the tail

(but still dominated by the slower particles), and the final stage in which all remaining particles in the droplet are of the type with faster isolated settling velocity. The mechanisms controlling each of these stages are explained. A similar segregation phenomenon related preferential transport of the slower particles into the droplet tail is observed in both the experiments and the numerical computations reported in the paper. Similar dynamics are observed for binary mixtures with different densities, binary mixtures with different particle sizes, and for mixtures with continuous distributions of particle size and density.

The essential problem examined in this paper concerns the inhibition of particle segregation by the hydrodynamic interaction of the particles in a situation where the particle terminal velocity differs within the mixture. This difference in terminal velocity acts to try to pull apart the mixture (enhancing segregation), whereas the hydrodynamic interaction acts to hold the mixture together (suppressing segregation). However, even in cases with strong hydrodynamic interaction, segregation can still occur within certain region of the mixture near the edges of the suspension droplet, and particularly near the droplet rear stagnation point. This basic problem occurs in many different particulate flow problems in which particle agglomerates or clusters are transported relative to the surrounding fluid. The model problem examined in the current paper should provide insight into the ability of clusters formed of a mixture of different particle sizes and densities to hold their structure even though differences in drag and other fluid forces act to tear apart the clusters.

If this work were to be continued in the future, one way that the work could be extended would be to use the same methods to study a falling suspension droplet that consists of a larger number of smaller particles. In the present experiments and computations a smaller number of larger particles were used in the suspension droplet. It has been shown in other studies that the behavior of a falling suspension droplet can be greatly affected by the number and size of the particles, and it would be interesting to do a separate study with the same methods used to examine the behavior of suspension droplets with these different characteristics. In addition, when studying the problem experimentally, PTV measurements could be used to help better understand the experimental flow field.

One of the limitations of the Oseen dynamics used in these computations is that it cannot be used with a flow field that has a bounded domain. It would be interesting to extend the Oseen dynamics so that it can be used with a bounded domain. Many applications of a falling suspension droplet involve boundaries (ie. Particulate inhalation into the lungs), and this would allow for the effects of a boundary on a falling suspension droplet to be studied.

Another addition that could be made if this study were to be continued, would be to implement a more robust method for solving the matrix equation (3.2). The current Gauss-Seidel iteration method causes the suspension droplet computations to be limited to lower concentrations, even though Oseen dynamics would otherwise allow for larger concentrations.

Finally, it would be interesting to use the concepts learned from this study to investigate ways in which segregation can be promoted, or how the rate of the vertical tail formation could be increased. Things such as the effects of acoustics impulses on the droplet could be investigated to see if they increase the segregation behavior.

References

Aarts PAMM, van den Broek SAT, Prins GW, Kuiken GDC, Sixma JJ, Heethaar RM. Blood platelets are concentrated near the wall and red blood cells, in the center in flowing blood. *Arterioscler* **8**, 819-824 (1988).

Adachi K, Kiriya S, Yoshioka N. The behavior of a swarm of particles moving in a viscous fluid. *Chemical Engineering Science* **33**(1), 115-121 (1978).

Asmar BN, Langston PA, Matchett AJ. A generalised mixing index in distinct element method simulation of vibrated particulate beds. *Granular Matter* **4**, 129-138 (2002).

Bosse T, Kleiser L, Härtel C, Meiburg E. Numerical simulation of finite Reynolds number suspension drops settling under gravity. *Physics of Fluids* **17**, 037101 (2005).

Bretherton FP. Inertial effects on clusters of spheres falling in a viscous fluid. *Journal of Fluid Mechanics* **20**(1), 401-410 (1964).

Brady J, Bossis G. Stokesian dynamics. *Annual Review of Fluid Mechanics* **20**, 111-157 (1988).

Chen H, Marshall JS. A Lagrangian vorticity method for two-phase particulate flows with two-way phase coupling. *Journal of Computational Physics* **148**, 169-198 (1999).

Cundall PA, Strack ODL. A discrete numerical model for granular assemblies. *Geotechnique* **29**(1), 47-65 (1979).

Ekiel-Jeżewska ML, Felderhof BU. Periodic sedimentation of three particles in periodic boundary conditions. *Physics of Fluids* **17**, 093102 (2005).

Ekiel-Jeżewska ML, Felderhof BU. Clusters of particles falling in a viscous fluid with periodic boundary conditions. *Physics of Fluids* **18**, 121502 (2006a).

Ekiel-Jeżewska ML, Metzger B, Guazzelli É. Spherical cloud of point particles falling in a viscous fluid. *Physics of Fluids* **18**, 038104 (2006b).

- Elghobashi S, Truesdell GC. On the two-way interaction between homogeneous turbulence and dispersed solid particles. I: Turbulence modification. *Physics of Fluids A* **5**, 1790-1801 (1993).
- Hadamard J. Movement permanent lent d'une sphere liquide visqueuse dans un liquid visqueux. *C.R. Acad. Sci. Paris Sér. A-B* **152**, 1735-1739 (1911).
- Hertz H. Über die Berührung fester elastische Körper. *J. reine und angewandte Mathematik* **92**, 156-171 (1882).
- Hocking LM. The behaviour of clusters of spheres falling in a viscous fluid. Part 2. Slow motion theory. *Journal of Fluid Mechanics* **20**, 129-139 (1964).
- Hurley P, Physick W, Lagrangian particle modelling of buoyant point sources: Plume rise and entrainment under convective conditions. *Atmospheric Environment A* **27**(10), 1579-1584 (1993).
- Jain N, Ottino JM, Lueptow RM. Regimes of segregation and mixing in combined size and density granular systems: an experimental study. *Granular Matter* **7**, 69-81 (2005).
- Jayaweera KOLF, Mason BJ, Slack GW. The behaviour of clusters of spheres falling in a viscous fluid. Part 1. Experiment. *Journal of Fluid Mechanics* **20**(1), 121-128 (1964).
- Kojima M, Hinch EJ, Acrivos A. The formation and expansion of a toroidal drop moving in a viscous fluid. *Physics of Fluids* **27**(1), 19-32 (1984).
- Kumar A, Graham MD. Margination and segregation in confined flows of blood and other multicomponent suspensions. *Soft Matter* **8**(41), 10536-10548 (2012).
- Leighton D, Acrivos A. The shear-induced migration of particles in concentrated suspensions. *Journal of Fluid Mechanics* **181**, 415-439 (1987).
- Li H, McCarthy JJ. Phase diagrams for cohesive particle mixing and segregation. *Physical Review E* **71**, 021305 (2005).
- Li HM, McCarthy JJ. Controlling cohesive particle mixing and segregation. *Physical Review Letters* **90**(18), 184301 (2003).
- Machu G, Meile W, Nitsche LC, Schaflinger U. Coalescence, torus formation and breakup of sedimenting drops: experiments and computer simulations. *Journal of Fluid Mechanics* **447**, 299-336 (2001).
- Marshall JS. Discrete-element modeling of particulate aerosol flows. *Journal of Computational Physics* **228**, 1541-1561 (2009).

- Marshall JS, Sala K, Comparison of methods for computing the concentration field of a particulate flow. *International Journal of Multiphase Flow* **56**, 4-14 (2013).
- Martonen, TB. Deposition patterns of cigarette-smoke in human airways. *American Industrial Hygiene Association Journal* **53**, 6-18 (1992).
- McHale G, Newton M, Shirtcliffe N. Immersed superhydrophobic surfaces: Gas exchange, slip and drag reduction properties. *Soft Matter* **6**, 714-719 (2010).
- Metzger B, Nicolas M, Guazzelli É. Falling clouds of particles in viscous fluids. *Journal of Fluid Mechanics* **580**, 283-301 (2007).
- Nitsche JM, Batchelor GK. Break-up of a falling drop containing dispersed particles. *Journal of Fluid Mechanics* **340**, 161-175 (1997).
- Noh Y, Fernando HJS. The transition in the sedimentation pattern of a particle cloud. *Physics of Fluids A* **5**(12), 3049-3055 (1993).
- Park J, Metzger B, Guazzelli É, Butler JE. A cloud of rigid fibres sedimenting in a viscous fluid. *Journal of Fluid Mechanics* **648**, 351-362 (2010).
- Phalen RF, Oldham MJ, Mannix RC, Schum GM. Cigarette-Smoke deposition in the tracheobronchial tree-evidence for colligative effects. *Aerosol Science and Technology* **20**, 215-226 (1994).
- Pignatel F, Nicolas M, Guazzelli É. A falling cloud of particles at a small but finite Reynolds number. *Journal of Fluid Mechanics* **671**, 34-51 (2011).
- Proudman I, Pearson JRA. Expansions at small Reynolds numbers for the flow past a sphere and a circular cylinder. *Journal of Fluid Mechanics* **2**(3), 237-262 (1957).
- Robinson RJ, Yu CP. Deposition of cigarette smoke particles in the human respiratory tract. *Aerosol Science and Technology* **34**, 202-215 (2001).
- Roeder RK, Steinlage GA, Trumble KP, Bowman KJ. Preventing segregation during centrifugal consolidation of particulate suspensions: particle drafting. *Journal of the American Ceramic Society* **78**(9), 2367-2373 (1995).
- Rybczynski W. Über die fortschreitende Bewegung einer flüssigen Kugel in einem zähen Medium. *Bull. Int. Acad. Sci. Cracov.* **1911A**, 40-46 (1911).

Shinohara K, Golman B. Segregation indices of multi-sized particle mixtures during the filling of a two-dimensional hopper. *Advanced Powder Technology* **13**(1), 93–107 (2002).

Subramanian G, Koch, DL. Evolution of clusters of sedimenting low-Reynolds-number particles with Oseen interactions. *Journal of Fluid Mechanics* **603**, 63-100 (2008).

Tsuji Y, Tanaka T, Ishida T. Lagrangian numerical simulation of plug flow of cohesionless particles in a horizontal pipe. *Powder Technology* **71**, 239-250 (1992).

Vasseur P, Cox RG. The lateral migration of spherical particles sedimenting in a stagnant bounded fluid. *Journal of Fluid Mechanics* **80**(3), 561-591 (1977).

Walther JH, Koumoutsakos P. Three-dimensional vortex methods for particle-laden flows with two-way coupling. *Journal of Computational Physics* **167**, 39-71 (2001).